Investigating the role of incident ion flux in solar wind space weathering of carbon-rich asteroidal regolith via H^+ and He^+ irradiation of the Murchison meteorite

Laczniak, D. L[1,*], Thompson, M. S[1], Christoffersen, R[2], Dukes, C. A[3], Morris, R. V[4], Keller, L. P[4]

[1]Department of Earth, Atmospheric, and Planetary Sciences, Purdue University, 550 Stadium Mall Drive, West Lafayette, IN 47907

[2]Jacobs, NASA Johnson Space Center, Mail Code X13, Houston TX 77058

[3]Laboratory for Astrophysics and Surface Physics, University of Virginia, 395 McCormick Road, Charlottesville, VA 22904

[4]ARES, Mail Code X13, NASA Johnson Space Center, Houston, TX 77058

*Corresponding author: dlacznia@purdue.edu; (702) 533-3878

Keywords (3-5): space weathering, carbonaceous asteroids, solar wind irradiation, Murchison

Abstract: We present results from a set of low and high flux 1 keV/amu H^+ and He^+ irradiation experiments performed on slabs of the Murchison CM2 carbonaceous chondrite. The low flux conditions for H^+ and He^+ irradiation were ~1-1.5 orders of magnitude lower than the high flux conditions, and each experiment was irradiated to a total fluence between ~3×10^{16} to ~6×10^{16} ions/cm^2. Irradiation-induced changes in the surface chemistry and optical properties of the Murchison samples were evaluated using *in situ* X-ray photoelectron spectroscopy (XPS) and visible and near-infrared spectroscopy (VNIR). We characterized the microstructure and composition of ion damaged rims in focused ion beam (FIB) cross-sections extracted from olivine and matrix material in each irradiated Murchison slab using transmission electron microscopy (TEM). XPS results suggest that both low flux and high flux H^+ and He^+ irradiation cause minor sputtering of surface carbon as well as a reduction in the valence state of iron, from Fe^{3+} to Fe^{2+}. Slope bluing is observed in VNIR spectra of the irradiated samples which may reflect carbonization and dehydrogenation of organic species and contrasts with reddening trends associated with npFe^0 formation. Although we do not observe a strong flux-dependence on the crystallinity of ion-damaged olivine, TEM analyses reveal a variety of microstructures in all olivine FIB-sections, suggesting that crystallographic orientation affects amorphization efficiency. Analyses of matrix FIB-sections indicate that phyllosilicate alteration is mainly driven by He^+ irradiation, where the higher incident flux leads to greater amorphization and the formation of more distinct ion-damaged layers, similar to smooth layers in returned Ryugu particles. TEM results also provide some evidence that higher ion flux leads to greater vesiculation, with He^+ irradiation being more efficient at vesiculation than H^+ irradiation, and that higher ion flux may promote the segregation of Mg and Si into laterally extensive lenses and layers in olivine samples. We discuss the implications of these findings for constraining the role that ion flux plays in the development of space weathering characteristics in silicate phases present in carbonaceous asteroidal regoliths. These results will be important for understanding the complexity of this process and how it operates on carbon-rich airless bodies like asteroids Bennu and Ryugu.

1. Introduction

Without the protection of an atmosphere, the surfaces of airless planetary bodies are continuously bombarded with high-speed, micrometer-sized dust particles (i.e., micrometeoroids) and energetic ions from the Sun (i.e., solar wind irradiation). Known collectively as space weathering, these processes alter the microstructural and chemical properties of the outermost ~100 nm of regolith grains and rocks exposed to the harsh environment of interplanetary space. As the physiochemical products of space weathering accumulate over time, the overall spectral signature of the regolith changes, complicating the interpretation of surface composition and mineralogy from remote-sensing observations and obscuring links between meteorites and their parent bodies (Hapke, 2001; Pieters and Noble, 2016). Employing a combination of laboratory experiments, returned sample analyses, and ground- and spacecraft-based spectroscopic investigations, we can examine the microstructural, chemical, and optical effects of space weathering in different environments to develop a comprehensive model of the space weathering process across the solar system.

Research over the last few decades has put important constraints on the effects of space weathering on the Moon and silicate-rich (S-type) asteroids. In the visible and near-infrared wavelength range (VNIR; 0.5 – 2.5 μm), progressive space weathering of these bodies has been shown to cause darkening (i.e., reduction in albedo), reddening (i.e., increasing reflectance with increasing wavelength), and attenuation of absorption bands (Abe et al., 2006; Hapke, 2001; Hiroi et al., 2006; Keller and McKay, 1997; Pieters et al., 2000; Taylor et al., 2001). Laboratory experiments and analyses of returned samples from the Moon and S-type asteroid Itokawa identified metallic Fe nanoparticles ($npFe^0$) formed via space weathering as the primary mechanism causing the observed spectral effects. Although $npFe^0$ is abundant in both lunar and Itokawa samples, recent studies have identified oxidized Fe nanoparticle phases including wüstite (Fe^{2+}) and magnetite in mature lunar soils (Thompson et al., 2016) and surface-correlated Fe-sulfide nanoparticles in space-weathered rims of Itokawa particles (Noguchi et al., 2011, 2014a, 2014b). Other characteristic physiochemical features of space weathering observed in lunar and/or Itokawa samples include partially to completely amorphous solar-wind damaged rims, nanocrystalline rims, vesiculated textures, near-surface cation depletion/enrichment, and re-deposition of melt and vapor material rich in elements not native to the host mineral (Keller and Mckay, 1997; Nakamura et al., 2011a; Keller and Berger, 2014; Noguchi et al., 2014a, 2014b; Thompson et al., 2014).

Although this work has built a detailed framework for space weathering on the Moon and S-type asteroids, there remain outstanding questions. One such question relates to the lack of complete amorphization in solar wind-damaged rims of returned lunar and Itokawa olivine grains. Numerical models and laboratory simulations of solar wind space weathering predict that olivine surfaces should become completely amorphous after exposure to ion irradiation fluences on the order of 10^{16} ions/cm^2 (Carrez et al., 2002; Chamberlin et al., 2008; Christoffersen et al., 2020; Christoffersen and Keller, 2015). Based on solar flare track and isotopic analyses, returned lunar grains have occupied the upper few millimeters of the lunar regolith for roughly 10^5-10^7 years and Itokawa grains for $<10^5$ years, respectively (Berger and Keller, 2015; Keller et al., 2021, 2016; Keller and Berger, 2014; Keller and Zhang, 2015). Assuming these grains remained in the upper ~100 nm of the regolith, which is the range of solar wind implantation, these exposure timescales correspond to ion fluences that *exceed* the 10^{16} ions/cm^2 critical amorphization dose of olivine, thus suggesting that returned olivine grain rims should be completely amorphous. Paradoxically, transmission electron microscope (TEM) studies of lunar and Itokawa returned samples reveal crystalline to nanocrystalline olivine rims that show a high

degree of lattice strain with abundant dislocations but few to no localized regions of amorphization (Burgess and Stroud, 2021; Harries and Langenhorst, 2014; Keller et al., 2021, 2016; Keller and Berger, 2014; Keller and McKay, 1997, 1993; Noguchi et al., 2014b, 2011; Thompson et al., 2014). In contrast, plagioclase grains returned from the same parent body and with similar exposure histories exhibit completely amorphous zones at or near their surfaces, observations which are consistent with predictions from laboratory experiments.

One potential explanation for the microstructural inconsistency between experimentally ion irradiated olivine and solar wind irradiated olivine is a difference in the flux of incident ions. The solar wind has an ion flux of 10^8 ions/cm^2/s at 1 AU (Johnson, 1990). However, ion irradiation experiments typically employ fluxes that are ~4-5 orders of magnitude higher than the solar wind (10^{12}-10^{13} ions/cm^2/s) to achieve relevant total fluences in reasonable time frames in the laboratory (e.g., Dukes et al., 1999; Loeffler et al., 2009; Matsumoto et al., 2015a; Takigawa et al., 2019; Keller et al., 2021; Laczniak et al., 2021). Although, historically, the effect of ion flux on lattice damage has been considered secondary to the effect of ion fluence, olivine may respond differently under different flux regimes. Low flux H^+ and He^+ ion irradiation experiments are needed to resolve the paradox of solar wind microstructural damage in experimentally irradiated versus naturally irradiated olivine grains.

Beyond the flux paradox, further outstanding questions in space weathering relate to how carbon-rich, or C-complex, asteroid surfaces are altered. C-complex asteroids are unique in that they contain both hydrated minerals and organic molecules (e.g., Zolensky et al., 1993; Sephton, 2002; Glavin et al., 2018). Over the past five years, the Japan Aerospace Exploration Agency (JAXA) Hayabusa2 and the NASA OSIRIS-REx missions collected samples from C-complex asteroids Ryugu and Bennu, respectively (Lauretta et al., 2021; Yada et al., 2021). Hayabusa2 successfully delivered ~5.4 g of Ryugu material to Earth (Yada et al., 2021), providing the scientific community with the first opportunity to examine pristine, organic-rich material from a C-complex asteroid directly in the laboratory. Analyses of Ryugu samples show evidence of space weathering by both solar wind irradiation and micrometeoroid bombardment (Nakato et al., 2023; Noguchi et al., 2022). Observations of amorphous phyllosilicate layers up to ~100 nm in thickness as well vesiculated and porous surface textures in multiple mineral phases (e.g., phyllosilicates, sulfides, magnetite, carbonates) suggest alteration by solar wind (Nakato et al., 2023; Noguchi et al., 2022). Additionally, the presence of amorphous melt layers and melt splashes up to several hundred nanometers in thickness indicate the occurrence of micrometeorite impacts (Nakato et al., 2023; Noguchi et al., 2022). Interestingly, npFe^0 is rarely found in Ryugu samples; rather, melt deposits contain abundant Fe- and Fe-Ni-sulfide nanoparticles (<200 nm) (Melendez et al., 2023; Noguchi et al., 2022; Thompson et al., 2022).

Prior to the availability of returned samples from Ryugu and soon, Bennu, scientists relied on laboratory experiments with carbonaceous chondrite analogs to investigate the effects of space weathering on carbon-rich bodies. These studies used ion irradiation to simulate solar wind radiation and pulsed laser irradiation or flash heating to simulate micrometeorite impacts. (e.g., Hapke, 1973; Bradley et al., 1996; Yamada et al., 1999; Dukes et al., 1999; Sasaki et al., 2001; Carrez et al., 2002; Moroz et al., 2004; Court et al., 2006; Loeffler et al., 2008, 2009; Court and Sephton, 2012; Brunetto et al., 2014; Lantz et al., 2015, 2017; Gillis-Davis et al., 2017; Thompson et al., 2019a, 2019b, 2020; Prince et al., 2020; Trang et al., 2021; Laczniak et al., 2021; Rubino et al., 2022; Chaves et al., 2023). Together, these studies indicate that space weathering of C-complex asteroids deviates from the canonical lunar model. Investigations focused on spectral space weathering changes in carbon-rich analogs show a weakening of

absorption bands in the VNIR wavelength range consistent with lunar observations. However, trends in spectral slope and albedo vary greatly with some studies showing reddening, others bluing, some brightening and others darkening (Brunetto et al., 2014; Brunetto and Strazzulla, 2005; Clark et al., 2023; Gillis-Davis et al., 2017, 2015, 2013; Hiroi et al., 2013; Kaluna et al., 2017; Lantz et al., 2017, 2015; Matsuoka et al., 2015; Prince et al., 2020; Thompson et al., 2020, 2019b; Vernazza et al., 2013).

Analyses of experimentally space weathered carbon-rich analogs revealed amorphization of phyllosilicates, highly vesiculated rims, elemental sputtering and segregation at the surface, formation of melt splashes and vapor layers, and the presence of very compositionally diverse Fe-bearing nanoparticles, such as Fe metal, Fe-sulfide, Fe-Ni sulfide, and Fe-oxide phases (e.g., Keller et al., 2015b, 2015c, 2015a; Gillis-Davis et al., 2017; Kaluna et al., 2017; Thompson et al., 2019b, 2020; Laczniak et al., 2021). Although these previous experimental investigations provide important insights into space weathering on C-complex asteroids, additional studies employing *coordinated* optical, microstructural, and chemical analytical techniques are imperative to correlate space weathering-induced changes in spectral properties to fully understand the complexities of space weathering of carbonaceous asteroidal regolith.

Realizing this need for additional studies specific to C-complex asteroids, coupled with outstanding questions regarding the role of flux in space weathering, we investigate how ion flux influences the solar wind space weathering of carbonaceous asteroidal regolith by performing a set of low flux and high flux 1 keV H^+ and 4 keV He^+ ion irradiation experiments on the Murchison CM2 carbonaceous chondrite. We integrate results from a suite of coordinated analytical techniques (X-ray photoelectron microscopy, VNIR spectroscopy, and electron microscopy) designed specifically to determine the spectral, microstructural, and compositional changes that result from low flux and high flux ion irradiation. Findings from this correlative experimental study will provide ground-truth for analyzing Ryugu and Bennu returned samples, help interpret Hayabusa2 and OSIRIS-REx orbital data, and improve grain exposure timescale models based on radiation damage

2. Samples and Methods

In this study, slabs of the Murchison (CM2) carbonaceous chondrite were used as an analog for carbon-rich asteroidal regoliths, as this meteorite is rich in organics and phyllosilicates and has a low optical albedo and featureless spectral signature in the VNIR wavelength range (Clark et al., 2011; Cloutis et al., 2011b; Hamilton et al., 2019; Simon et al., 2020). From the allocated Murchison stones, we prepared four dry-cut, flat slabs measuring roughly 10 mm × 10 mm. Prior to irradiation, slab surfaces were roughened with 400 grit silicon carbide grinding paper to limit spectral reflection (Laczniak et al., 2021).

2.1 Ion irradiation experiments

The surface of each Murchison slab was irradiated with either 1 keV H^+ or 4 keV He^+ in an ultra-high vacuum chamber (10^{-8} Pa) at the University of Virginia's (UVA) Laboratory for Astrophysics and Surface Physics. A set of low flux/low fluence and high flux/low fluence experiments were performed, which are hereafter abbreviated as LF/LF and HF/LF, respectively. LF/LF He^+ irradiation used an average flux of 3.6×10^{11} $He^+/cm^2/s$ and reached a total fluence of 2.1×10^{16} He^+/cm^2 (~400 years of exposure at Bennu); LF/LF H^+ irradiation used an average

flux of 6.6 × 10^{11} $H^+/cm^2/s$ and reached a total fluence of 3.9 × 10^{16} H^+/cm^2 (~30 years of exposure). HF/LF He^+ irradiation used an average flux of 9.1 × 10^{12} ions/cm^2/s and reached a total fluence of 2.0 × 10^{16} ions/cm^2 (~400 years of exposure); HF/LF H^+ irradiation used an average flux of 8.4 × 10^{12} ions/cm^2/s and reached a total fluence of 5.8 × 10^{16} ions/cm^2 (~50 years of exposure). Achieving similar total fluences in both the LF and HF experiments allows us to better isolate and evaluate the effects of ion flux. The incident ion beams were oriented perpendicular to the surface of the Murchison slabs and rastered over a rectangular area ≥ 4 x 7 mm^2. Average fluxes were determined from Faraday cup measurements before and after each irradiation. During the irradiation, electrostatic charging of the surface was mitigated with continuous operation of an electron neutralizer with a 20 μA emission current of low energy electrons (<1 eV). The exposure times for each experiment were determined using estimates of the ion fluxes at 1.126 AU (the semimajor axis of Bennu's orbit) which we calculated to be ~1.5 × 10^8 $H^+/cm^2/s$ and ~6.4 × 10^6 $He^+/cm^2/s$, respectively.

2.2 X-ray photoelectron spectroscopy (XPS)

We performed X-ray photoelectron spectroscopy (XPS) using a micro-focused, monochromatic, Al k-alpha X-ray beam (1486.6 eV) under ultra-high vacuum (10^{-7}-10^{-8} Pa) to determine quantitative changes in the surface chemistry of the Murchison slabs (topmost ~10 nm). Using the PHI Versaprobe III Scanning XPS Microprobe at Uva, survey and high-resolution XPS spectra were acquired in situ, from the same sample locations, before and after ion irradiation in several fluence increments. At least three points were analyzed during each irradiation experiment, as is shown in figure S1. Due to the diminished photoelectron count rates at relatively small (10-20 μm) spot sizes, X-rays were focused to 100 or 200 μm. As a result, completely isolating either chondrule or matrix material with the XPS beam was difficult, and each spectrum likely contains contributions from both materials.

High-resolution analyses examined the O-1s, C-1s, S-2p, Al-2p, Si-2p, Mg-2s, and Fe-2p binding energy regions to investigate fluence-induced changes in surface chemistry. The hemispherical electron energy analyzer was operated at a fixed pass energy of 280 eV for survey spectra and 55 eV for high resolution spectra, providing instrument energy resolutions of 2.7 eV and 0.5 eV, respectively. Differential surface charging during XPS analysis was mitigated with continuous dual-beam charge neutralization.

2.3 Visible and near-infrared (VNIR) spectroscopy

Visible and near-infrared spectroscopy (VNIR; 0.35-2.5 μm) was performed at NASA Johnson Space Center (JSC) with a fiber-optic ASD FieldSpec 3 Hi-Res Spectroradiometer. This instrument is equipped with a Muglight probe which has a spot size of ~7 mm, an incidence angle of 35˚ (with respect to the surface normal), an emission angle of 12˚ (with respect to the surface normal), and a phase angle of 23˚. Under ambient laboratory conditions, we acquired absolute reflectance spectra from the low flux slab surfaces *after* irradiation and from the high flux slab surfaces *both before and after* irradiation. During high flux VNIR acquisition, care was taken to ensure the same area of the Murchison sample was analyzed before and after the irradiation experiment.

A Labsphere Spectralon white standard (~99% Lambertian reflectance) was used for calibration. Final low flux spectra represent the average of at least 60 measurements, total,

collected at varying azimuth angles (0˚, 90˚, 180˚, and 270˚). Final high flux spectra are the average of 4 measurements taken at the same 90˚ rotations. We did not observe any systematic effects in the spectral band centers or intensities as the azimuthal orientation was varied. Continuum-removed spectra were computed from absolute reflectance using built-in functions in the Harris Geospatial Solutions Environment for Visualizing Instruments (ENVI) program.

2.4 Focused ion beam scanning electron microscopy (FIB-SEM) and field-emission scanning transmission electron microscopy (FE-STEM)

We used focused ion beam scanning electron microscopy (FIB-SEM) to extract electron transparent (<100 nm) cross-sections (hereinafter referred to as FIB sections) from an olivine grain and a phyllosilicate-rich matrix region in each of the four ion-irradiated Murchison slabs, yielding eight FIB sections in total. The Thermo Scientific Helios G4 UX Dual Beam FIB-SEM at Purdue and the FEI Quanta 3D FIB-SEM at JSC were used for FIB section extraction. The ion irradiated surface of these FIB sections was protected from ion beam damage during sample preparation by the deposition of a thick carbon strap (≥ 2 μm) over areas of interest, prior to milling. All final FIB sections are ≥8 μm in depth and, thus, include both ion-affected material near the surface and unaltered material below, allowing differences in microstructure and composition to be observed with TEM techniques within the same sample.

Each FIB section was analyzed with TEM and energy dispersive X-ray spectroscopy (EDS) at Purdue and JSC. Purdue houses a Thermo Fisher Talos F200X G2 field-emission scanning transmission electron microscope (FE-STEM) equipped with four windowless Super-X silicon drift detectors. JSC houses a JEOL 2500 SE 200 kV FE-STEM equipped with a JEOL SD60GV 60 mm^2 ultra-thin window silicon drift detector. A combination of conventional bright field TEM (BF TEM), high-resolution TEM (HRTEM), bright field scanning TEM (BF STEM), and high-angle annular dark field STEM (HAADF) images were obtained. Element abundances and distributions were investigated with EDS spot analyses, element maps, and line profiles. Quantification of element maps and line profiles was carried out in the Velox or Thermo NSS software using the standards-based Cliff-Lorimer method.

3. Results

3.1 X-ray photoelectron spectroscopy (XPS)

Survey XPS spectra show the presence of C, O, Na, Mg, Al, Si, S, Fe, Ni and/or Cl in the uppermost ~10 nm of all analyzed matrix and chondrule regions in the LF/LF and HF/LF ion irradiated samples. Atomic concentrations of these elements before and after ion irradiation are summarized in the Appendix (Tables S1 and S2). Overall, only minor differences in the surface chemistry of chondrule and matrix regions were observed following LF/LF and HF/LF H^+ and He^+ irradiation, with the most significant changes being a reduction in C content, and sometimes O and S content, by preferential sputtering (Fig. 1 and Tables S1 and S2). Minor depletions (<1.0 atomic %, or at%) in other elemental abundances also occur, however, these changes are not consistent between multiple survey spectra from the same sample or across different samples (e.g., S, Ca, Ni, Cl). The abundances of all other elements either increase proportionally with the removal of C and O or are consistent with pre-irradiation concentrations.

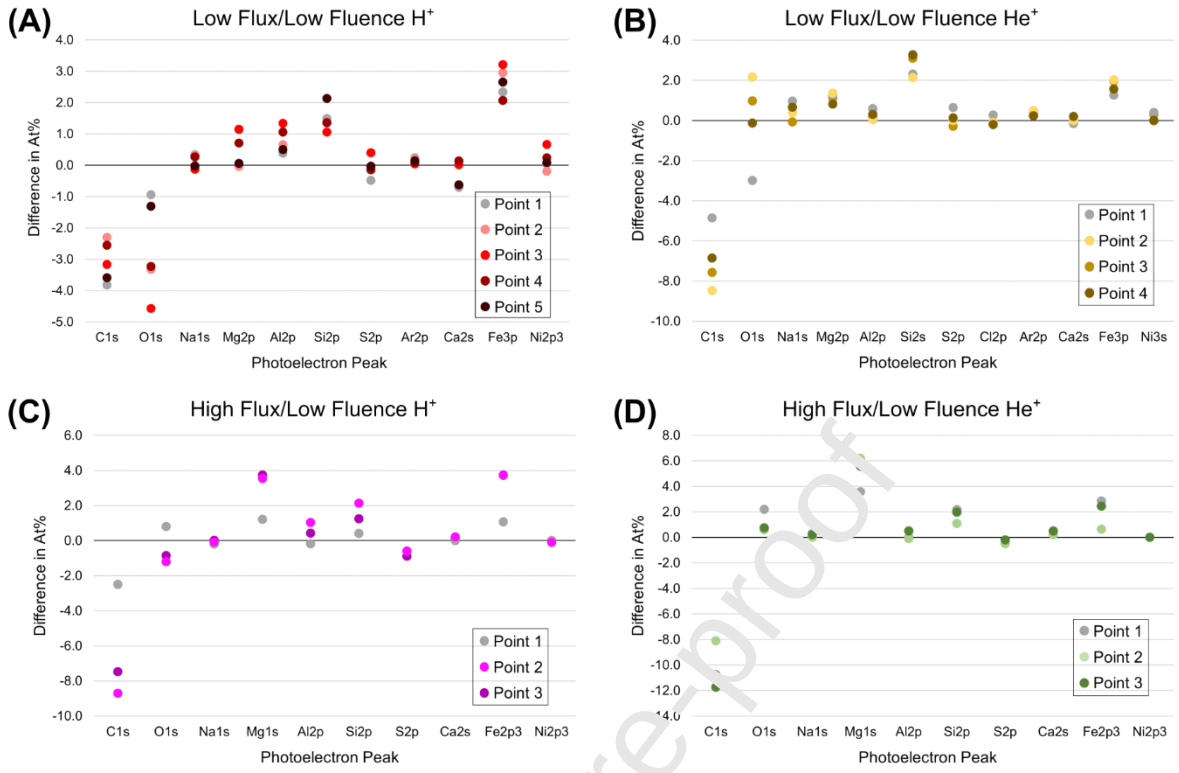

Figure 1. Plots showing the difference in elemental abundances (in atomic percent, or at%) derived from survey XPS spectra acquired before and after (A) LF/LF H^+ irradiation (red gradient), (B) LF/LF He^+ irradiation (yellow gradient), (C) HF/LF H^+ irradiation (magenta gradient), and (D) HF/LF He^+ irradiation (green gradient). The photoelectron peaks used for quantification of each element are listed along the x-axis. The bold line at 0.0 at% is unity and represents no change in elemental abundance after ion irradiation. Points that plot above unity represent an increase in the abundance of that element while points below unity represent a decrease. Each point corresponds to a different XPS analytical location. The average analytical error for each elemental difference is as follows: C (±0.81), O (±0.70), Na (±0.07), Mg (±0.24), Al (±0.35), Si (±0.17), S (±0.07), Ca (±0.11), Fe (±0.07), Ni (±0.07). These errors, which are derived from the average standard deviation across all XPS analysis points, are applicable to all four irradiation experiments.

XPS shows that each ion irradiated sample exhibits a slight decrease in C abundance which is consistent across three or more locations in each irradiated region and both matrix and inclusions. In the LF/LF samples, H^+ irradiation caused C abundance to decrease by ≤3.6 (at%) while He^+ irradiation caused C abundance to decrease by ≤8.5 at% (Fig. 1A and 1B). In the HF/LF experiments, H^+-irradiation lowered C by ≤6.7 at% and He^+-irradiation by ≤11.7 at% (Fig. 1C and 1D). He^+ irradiation yields a slightly greater reduction in C content compared to H^+ irradiation in both the low flux and high flux experiments. Similarly, ion irradiation decreases O abundance in the low flux experiments, while there was minimal variation (+/-1–2%) in the high flux results. In the LF/LF H^+-irradiated sample, O content decreases by ≤3.3 at%, with a greater reduction occurring in chondrule rather than matrix-dominated analysis points (Fig. 1A). Interestingly, a notable reduction in O content is observed in only one survey spectrum from the

LF/LF He^+-irradiated sample (a decrease of ~3.0 at%) (Fig. 1B). In the HF/LF samples, small (<2%) systematic changes in the O content with fluence were observed—both increasing and decreasing—along with a systematic decrease in the S content with both 1 keV H and 4 keV He (~50% decrease). Commensurate increases in Mg, Si, Ca, and Fe were observed in all locations within the impacted area for the HF/LF irradiations.

High-resolution XPS spectra reveal changes in peak binding energies derived from ion irradiation that correspond to differences in the elemental bonding environment (e.g., oxidation state). An example and explanation of the peak fitting procedure can be found in the supplementary material (Fig. S2). Peak fitting of high-resolution spectra from the C1s photoelectron region shows a prominent peak at ~284.8 eV associated with C-C/C-H bonds (Fig. 2). The unirradiated Murchison surface carbon consists of macromolecular material dominated by aromatic functionality (Barr and Seal, 1995; Vander Wal et al., 2011) and oxygenated carbon species at ~286.2 eV (C-O-C) and ~288.6 eV (O-C=O) (Fig. 2). Consistent with survey XPS results, these three carbon peaks weaken with progressive LF/LF and HF/LF H^+ and He^+ irradiation, indicating that sputtering results in a decrease in the overall surface C content. Oxygenated carbon peaks are essentially absent after all ion irradiation experiments. Interestingly, LF/LF and HF/LF H^+ irradiation causes the C-C/C-H peak to shift slightly towards a higher binding energy. No notable peak change was observed in the high flux He^+-irradiated high-resolution XPS spectra.

Examination of the Fe-2p photoelectron region reveals a small but detectable ion irradiation-induced change in iron oxidation state (Fig. 2). Using fitting parameters from Biesinger et al. (2011), we resolved the high-resolution spectra from this region into its $Fe2p_{1/2}$ and $Fe2p_{3/2}$ spin couplet components. Fig. 2 shows the $Fe2p_{3/2}$ spectra from each experiment. The prominent composite peak present in all $Fe2p_{3/2}$ (spin couplet) high-resolution spectra consists of a complex mixture of Fe^{3+} and Fe^{2+} multiplet-splitting features. The Fe^{3+} multiplet structure suggests that Fe^{3+} occurs in oxide and phyllosilicate phases. The Fe^{2+} multiplet structure suggests that Fe^{2+} occurs in phyllosilicates and olivine. After LF/LF and HF/LF H^+ and He^+ irradiation, a minor amount of Fe^{3+} is chemically reduced to Fe^{2+}. This reduction is represented by a shift in the primary composite peak towards a lower binding energy (Fig. 2). Iron is not reduced to Fe^0 in these experiments, as evident by the lack of a peak at ~706.5 eV corresponding to either metallic Fe (Fe-Fe) or sulfides (Fe-S) following irradiation (Biesinger et al., 2011; Terranova et al., 2018; Thomas et al., 2003). We did not identify any significant changes in surface chemistry in the Mg-2s, Al-2p, Si-2p, or O-1s photoelectron features.

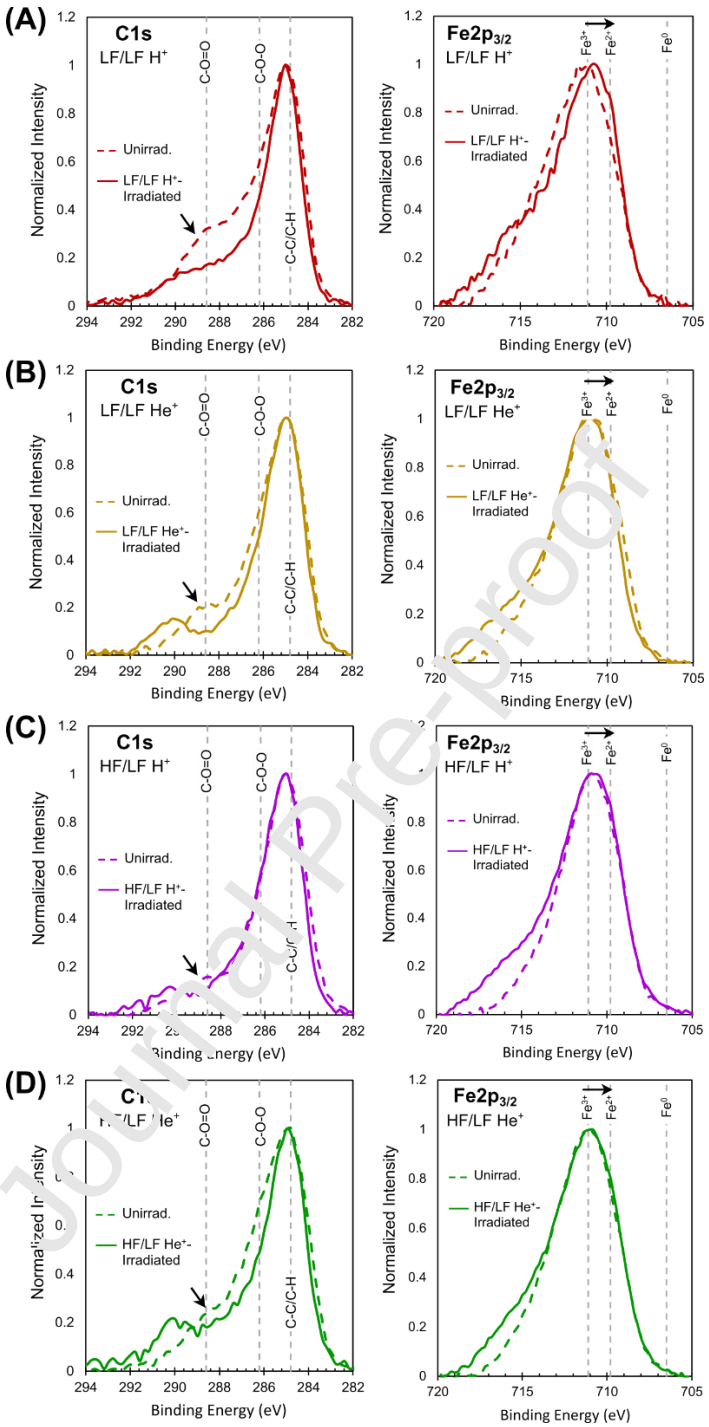

Figure 2. Normalized high-resolution (HR) XPS spectra showing changes in Murchison surface chemistry over the C1s and $Fe2p_{3/2}$ photoelectron regions before (dashed line) and after (solid line) each ion irradiation experiment. (A) Spectra from the LF/LF H^+ irradiation experiment (red). (B) Spectra from the LF/LF He^+ irradiation experiment (yellow). (C) Spectra from the HF/LF H^+ irradiation experiment (magenta). (D) Spectra from the HF/LF He^+ irradiation experiment (green). In all panels, the dashed line represents the unirradiated spectrum (abbreviated unirrad. in the legends) and the solid line represents the final irradiated spectrum. Black arrows call attention to changes in the spectra derived from ion irradiation.

3.2 Visible and near-infrared (VNIR) spectroscopy

The overall shape and low albedo (<7.5%) of the absolute reflectance spectra acquired from this study resembles previously published Murchison VNIR spectra (Fig. 3A) (e.g., Cloutis et al., 2011; Lantz et al., 2015; Thompson et al., 2019b, 2020; Laczniak et al., 2021). Their low albedo results from the abundant opaque phases present in Murchison (i.e., magnetite, tochilinite, sulfides, carbon species) (e.g., Johnson and Fanale, 1973; Milliken and Mustard, 2007; Cloutis et al., 2011a, 2011b, 2012). Because unirradiated VNIR spectra were not obtained from the LF/LF slabs prior to the ion irradiation experiments, here, we compare the LF/LF H^+ and He^+ irradiated spectra to an unirradiated Murchison spectrum acquired previously by Laczniak et al. (2021) from a different meteorite slab that was cut from the same bulk stone. Alternatively, for the HF/LF H^+ and He^+ irradiation experiments, reflectance spectra were acquired from the same region of each slab before and after ion irradiation, and thus, these unirradiated and irradiated spectra are compared to each other. Table 1 summarizes the slopes (defined over the 0.65-2.5 µm wavelength range) and albedos at different wavelengths of our unirradiated, LF/LF irradiated, and HF/HF irradiated spectra. Overall, we observe relatively minor changes in slope, albedo, and absorption band strength as a result of ion irradiation.

The albedos of the LF/LF H^+ and He^+-irradiated spectra are higher than the albedo of the unirradiated spectrum, with the H^+-irradiated spectrum exhibiting the highest reflectance (Fig. 3A). Locations of highest albedo in both the LF/LF H^+ and He^+ irradiated spectra are shifted shortward compared to the unirradiated spectrum, occurring at 0.53 µm in the former and 0.55 µm in the latter. Additionally, the LF/LF He^+-irradiated spectrum exhibits a similar slope compared to the unirradiated spectrum while the LF/LF H^+ irradiated spectrum exhibits a bluer slope (by ~25%). Compared to their unirradiated counterparts, the HF/LF H^+- and He^+- irradiated absolute reflectance spectra exhibit a slightly higher albedo at shorter wavelengths, specifically between ~0.35-2.10 µm (reflectance at 0.55 µm increases by ~2% and ~5%, respectively), leading to an overall bluing of their spectral slopes (Fig. 3A). HF/LF He^+ irradiation yields greater brightening at these shorter wavelengths, and, thus, greater slope bluing (by ~31%). The location of highest albedo also does not change following HF/LF H^+ and He^+ irradiation, occurring at ~0.55 µm in all these spectra.

Examination of continuum removed reflectance spectra from this study reveals many absorption features that are characteristic of the primary components of Murchison (Fig. 3B). Most prominent is the broad band between ~0.6-1.6 µm which reflects the superposition of absorptions bands associated with Fe-bearing minerals such as serpentines, olivine, ferrihydrite, and/or magnetite. In the unirradiated spectra, LF/LF He^+-irradiated spectrum, and HF/LF H^+- and He^+-irradiated spectra, this broad band is dominated by serpentine reflectance features, including the ~0.75 µm absorption associated with the Fe^{2+}-Fe^{3+} charge transfer and the ~0.90-0.95 and ~1.1-1.2 µm absorptions associated with octahedral Fe^{2+} crystal field transitions (Cloutis et al., 2012, 2011b, 2011a). Interestingly, the short wavelength region of the broad band in the LF/LF H^+-irradiated spectrum is dominated by a strong absorption at ~0.85 µm which may correspond to the Fe^{2+} crystal field transition in olivine's M1 crystallographic site or the Fe^{3+} spin forbidden transition in ferrihydrite (Cloutis et al., 2012, 2011b, 2011a). HF/LF H^+ irradiation does not notably alter the shape or strength of the broad band. However, HF/LF He^+ irradiation appears to slightly strengthen the absorption of this broad band, especially at ~0.91 µm and 1.13 µm (by ~1% for each). Additionally, all spectra exhibit an absorption feature at ~2.2-2.3 µm that is suggestive of metal-OH bonds in amorphous phases and/or phyllosilicates (Cloutis et al., 2012,

2011b). An absorption band at ~1.95 µm (OH^-/H_2O) also is present in all spectra which likely represents the hydrated phyllosilicate component within Murchison and/or atmospheric water adsorption resulting from acquisition of VNIR spectra under ambient laboratory conditions (Fig. 3C) (e.g., Beck et al., 2010; Cloutis et al., 2011a, 2011b, 2012; Takir et al., 2013; Lantz et al., 2015; Bishop et al., 2017). However, no change in this feature is observed following ion irradiation.

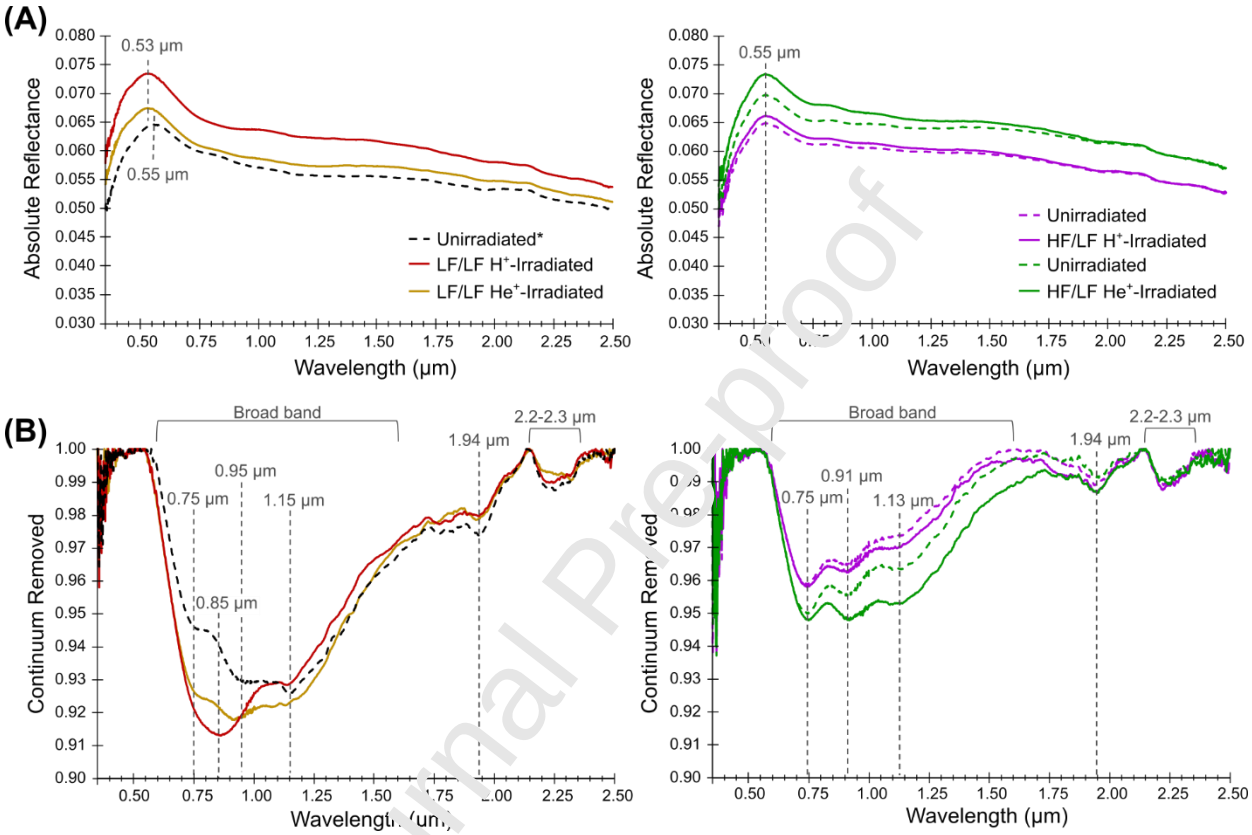

Figure 3. (A) Absolute reflectance spectra and (B) continuum removed reflectance spectra over the visible and near-infrared wavelength range (0.35-2.5 µm). Left panels show results from the LF/LF irradiation experiments, with the H^+-irradiated surface in red and the He^+-irradiated surface in yellow. Note that the unirradiated Murchison spectrum from Laczniak et al. (2021) is also included for comparison and represented by the dashed black line (and denoted by an asterisk in the legend). Right panels show results from the HF/LF experiments, with the H^+-irradiated surface in magenta and the He^+-irradiated surface in green. All unirradiated spectra are represented by dashed lines and irradiated spectra with solid lines.

Table 1. Albedo and slope values of the unirradiated, LF/LF irradiated, and HF/LF irradiated samples. The average standard deviation (1σ) over all wavelengths is also provided. Albedo and slope values from the unirradiated spectrum in Laczniak et al. (2021) are also listed for comparison to the LF/LF H^+- and He^+- irradiated spectra from this study.

	Low Flux, Low Fluence			High Flux, Low Fluence			
	Unirradiated	H^+-	He^+-	Unirradiate	H^+-	Unirradiate	He^+-

	*	irradiated	irradiated	d	irradiated	d	irradiated
		d	d		d		d
Reflectance at 0.35 μm	0.050 ± 0.003	0.058 ± 0.004	0.054 ± 0.003	0.050 ± 0.002	0.050 ± 0.003	0.053 ± 0.002	0.054 ± 0.003
Reflectance at 0.55 μm	0.065 ± 0.003	0.073 ± 0.004	0.067 ± 0.003	0.065 ± 0.002	0.066 ± 0.003	0.07 ± 0.002	0.073 ± 0.003
Reflectance at 2.50 μm	0.050 ± 0.003	0.054 ± 0.004	0.051 ± 0.003	0.053 ± 0.002	0.052 ± 0.003	0.057 ± 0.002	0.057 ± 0.003
Spectral Slope from 0.65 - 2.5 μm	-0.0067	-0.0084	-0.0068	-0.0054	-0.0060	-0.0055	-0.0072
Spectral Slope from 0.35-0.55 μm	0.0737	0.0771	0.0653	0.0763	0.0810	0.0860	0.0972

*Unirradiated Murchison spectrum from Laczniak et al. (2021)

3.3 Field-emission scanning transmission electron microscopy

The following section details results from TEM and EDS analysis of the olivine and matrix FIB-sections extracted from each of the ion irradiation experiments performed in this study (eight FIB-sections, total). Table 2 summarizes the microstructural and compositional characteristics of each FIB-section.

3.3.1 H^+-irradiated olivine samples

3.3.1.1 Low flux/low fluence (LF/LF) H^+-irradiated olivine. The ion-damaged surface of the LF/LF H^+-irradiated olivine sample exhibits variation in its microstructural characteristics. Some regions are highly strained but still completely crystalline (Fig. 4C) while others exhibit nanocrystalline domains and zones of partial amorphization in addition to remnants of the original olivine crystal structure (Fig. 4B). While the boundary between the ion-damaged surface

and unaltered olivine is not always well-defined, where it is clearly delineated, the ion-altered zone tends to extend between 30-60 nm below the surface. When present, partial amorphization usually occurs as small, randomly distributed pockets ≤10 nm in size. Occasionally, these amorphous pockets form more elongated islands that are roughly parallel to the sample surface (Fig. 4B). Although the degree of partial amorphization varies laterally in the damaged rim, nanocrystalline or crystalline domains always dominate.

BF TEM images also show the presence of small (~2-5 nm) spherical to oblong features distributed randomly within the ion-altered surface. These features are likely nanovesicles or defects. We also observe light contrast features in BF TEM images that are elongated, linear or undulating in morphology, and range in length from ~10-50 nm (Fig. 4A). While most are oriented roughly parallel to the sample's surface, some features are oriented nearly orthogonal. These elongated features appear similar to defects observed in some returned lunar and Itokawa olivine particles, which will be discussed in more detail in Section 4.2.1 (e.g., Burgess and Stroud, 2021; Cymes et al., 2022).

EDS analysis shows that this sample exhibits a continuous, chemically distinct layer in the outermost ~10 nm that is enriched in Mg, significantly depleted in Si, and slightly depleted in O (Fig. 4D, 4E, and S3). Typically, the Mg content in this layer exceeds the Mg content in the unaltered olivine (by ~17 at%) and the Si content decreases (to ≤10 at%). Following this surface layer, segregation between Mg and Si is observed up to 80 nm below the surface, forming randomly distributed patches of relative Mg enrichment/Si depletion and vice versa (Fig. S3). In some areas, the segregation of Mg and Si forms elongated lenses roughly parallel to the sample's surface, as in Fig. 4D. Within this larger zone of segregation, O content also is slightly enriched in some cases. Although Fe abundance is low, overall, in this olivine grain (~3 at%), it tends to segregate with Mg.

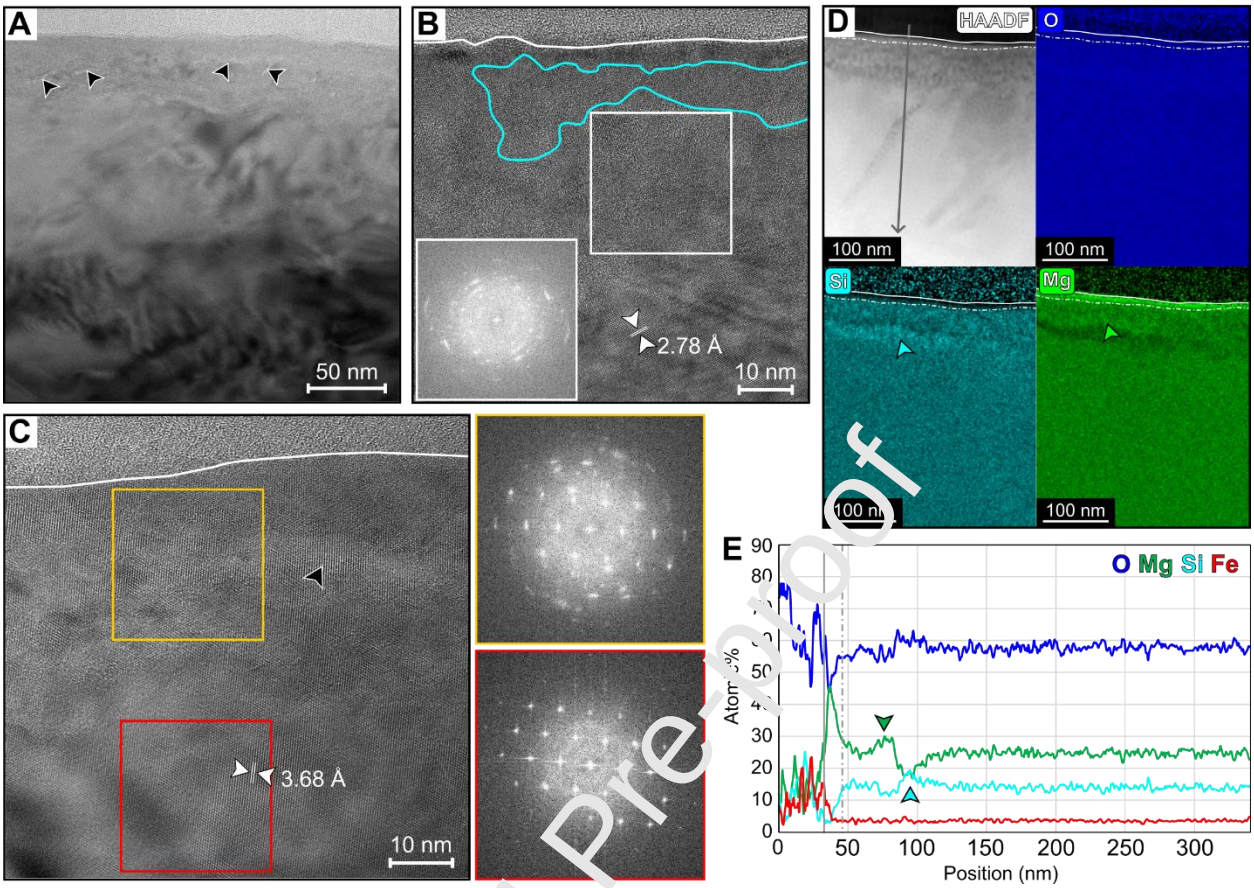

Figure 4. TEM imaging and microanalysis of the LF/LF fluence H^+-irradiated olivine sample. (A) BF TEM image showing the ion-damaged surface. Black arrows point to the thin, elongated light-contrast features. (B) An HRTEM image showing an elongated amorphous island (cyan outline) within the predominantly polycrystalline ion-altered surface. The inset FFT confirms the polycrystalline microstructure of the region. The measured d-spacing of 2.78 Å is also indicated and corresponds to the {130} family of planes. (C) HRTEM image showing a damaged but still crystalline region of the surface. The FFTs at the right confirm the crystalline nature of the surface (yellow outline) compared to the unaltered olivine (red outline). The measured d-spacing of 3.68 Å is also indicated and corresponds to the {101} family of planes. (D) Quantitative EDS map set (O in blue, Si in cyan, and Mg in green) and its corresponding HAADF image showing the segregation of Si and Mg into elongated lenses. The green arrow indicates a Mg-enriched, Si-depleted lens and the cyan arrow indicates a Si-enriched, Mg-depleted lens. The dotted-dashed line represents the base of the very Mg-rich and Si-poor surface layer. (E) A quantified elemental concentration profile extracted from the gray arrow in (D). Enrichments highlighted by the green and cyan arrows correspond to the elongated segregation layers observed in (D). For all panels, solid white lines denote the surface of the sample.

3.3.1.2 High flux/low fluence (HF/LF) H^+-irradiated olivine. The HF/LF H^+-irradiated olivine sample is characterized by a highly strained, but predominantly crystalline rim that is ~30 nm thick (Fig. 5A and 5B). Fast Fourier transform images (FFTs) extracted from the ion-damaged surface exhibit more diffuse reflections compared to the sharp reflections characteristic of the unaltered olivine. These FFTs also show evidence of some low-angle grain boundaries

(Fig. 5C). There are also rare, small pockets (~1-8 nm) of amorphous material sporadically distributed within this surface layer. Additionally, in the uppermost ≤5 nm of some areas, a light contrast, laterally discontinuous layer with possible partial amorphization is observed (Fig. 5B and 5C).

Similar to the LF/LF H^+-irradiated sample, we observe spherical to oblong light contrast features (mostly 2-5 nm in size) scattered throughout the ion-damaged rim (Fig. 5A). The density of these features, which are possible nanovesicles or defects, is higher in this sample compared to the LF/LF H^+-irradiated sample. The surface of this sample also contains thin, elongated, linear to undulating features that are oriented approximately parallel to the surface (Fig. 5B and 5C).

Compositional changes vary laterally in the HF/LF H^+-irradiated olivine grain. In some regions, no difference in Mg, Fe, Si, or O abundances are observed between the highly strained surface layer and the unaltered olivine. However, in other locations, O content increases and Mg content gradually decreases while Si content remains unchanged in the outermost 35-45 nm. Fe abundance slightly decreases until ~20 nm below the sample surface, at which depth its abundance begins to increase slightly, creating a trough-like feature in the EDS line profile (Fig. 5F). The lowest Fe abundance consistently occurs between 20-25 nm below the sample surface, creating a band that is relatively Fe-poor. Localized regions also exhibit a laterally discontinuous surface layer where the outermost ~5-10 nm is depleted in Si and slightly enriched in Mg and Fe (Fig. 5E and 5F).

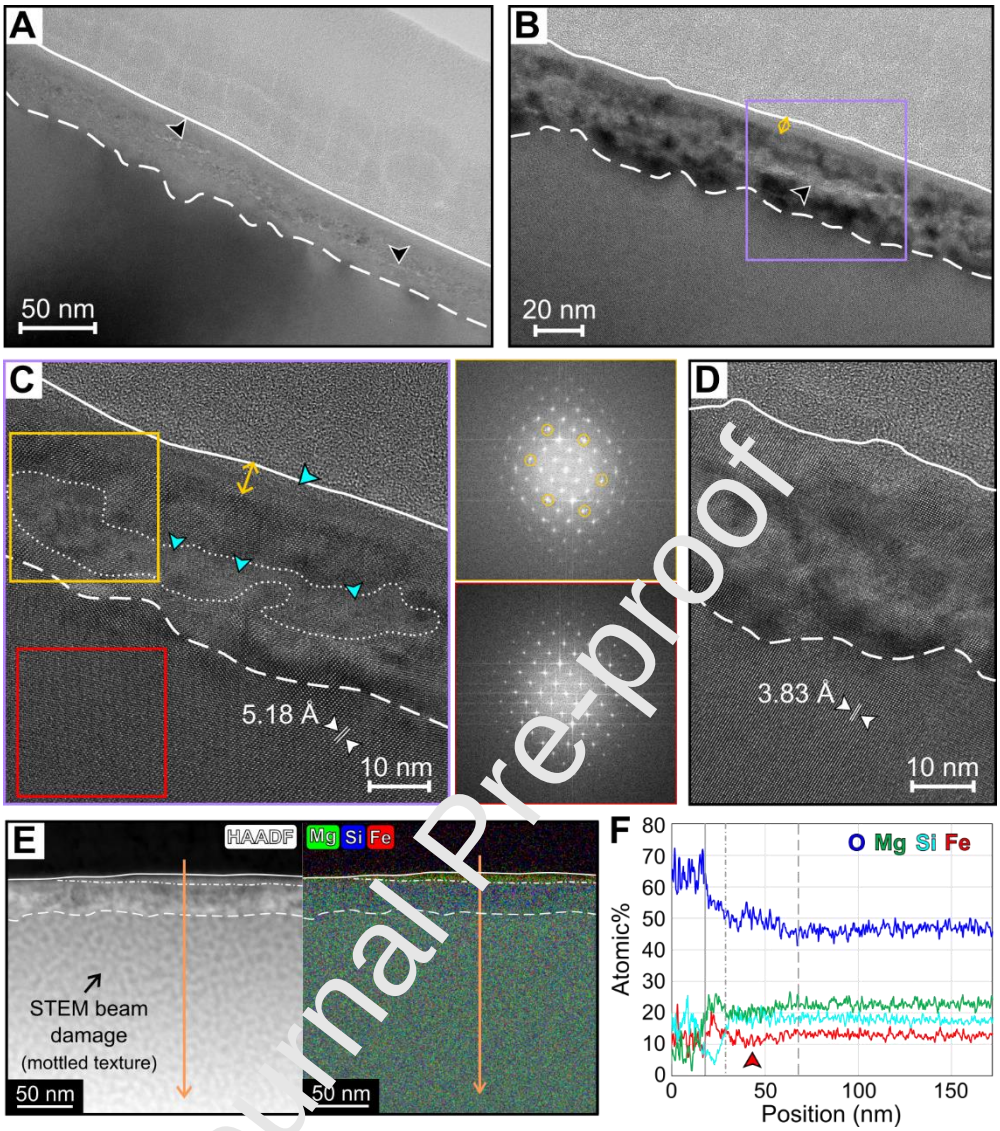

Figure 5. TEM imaging and microanalysis of the HF/LF H^+-irradiated olivine sample. (A) Conventional BF TEM image of the ion-affected surface. Black arrows indicate potential elongated structural defects. (B) A higher magnification BF TEM image acquired at a tilt that highlights a ~5 nm thick light contrast layer at the uppermost surface of the sample in this region (yellow double-sided arrow). (C) HRTEM image of the area outlined in purple in (B). The outer ~5 nm light contrast layer (double-sided yellow arrow) exhibits some partial amorphization. The remainder of the ion-damaged layer is strained but crystalline, as indicated by the FFTs at the right which were acquired from the surface (yellow boxes) and unaltered olivine (red boxes). Yellow circles in the yellow-outlined FFT encompass reflections indicative of low-angle grain boundaries. Cyan arrows point to amorphous pockets. Also note the elongated feature indicated by a dotted line in the HRTEM image. A measured d-spacing of 5.18 Å is also indicated and corresponds to the {011} family of planes. (D) An HRTEM mosaic showing a region of the ion-altered surface that lacks amorphous pockets and the ~5 nm light-contrast, partially amorphous upper layer. A measured d-spacing of 3.83 Å is also indicated and corresponds to the {021} family of planes. (E) HAADF image (left panel) and quantitative EDS map overlay showing the distribution of Mg (green), Si (blue), and Fe (red). The dot-dashed line indicates the base of a Si-

depleted layer. The mottled texture observed in the unaltered olivine substrate (below the dashed white line) reflects STEM beam damage from EDS analysis. (F) A quantified elemental concentration profile extracted from the orange arrow in (E). The red arrow highlights the depth at which Fe content is lowest. For all panels, solid white lines denote the surface of the sample and dashed white lines denote the boundary between the ion-damaged surface and unaltered olivine substrate.

3.3.2 He^+-irradiated olivine samples

3.3.2.1 Low flux/low fluence (LF/LF) He^+-irradiated olivine. The LF/LF He^+-irradiated olivine exhibits localized vesiculation within ~10-35 nm of the sample's surface. Vesicle shapes range from spherical to ovoid to oblong in shape and their sizes are usually ≤15 nm in length (Fig. 6A and 6B). The lower boundary of the ion-altered surface is not always well-defined, but in areas where a more distinct boundary was identified, microstructural damage reached depths of 20-65 nm. The microstructure of the surface of this sample varies laterally. Some regions exhibit partial amorphization embedded within crystalline material, while other regions are partially amorphous with islands of nanocrystallinity (Fig. 6C, 6F, and 6G). FFTs suggest that, in certain areas, amorphous material dominates, however, at least a minor amount of crystalline or nanocrystalline material is always maintained. Additionally, some regions have a very localized, laterally discontinuous outer layer (~7-10 nm) that is lighter in contrast in BF TEM and mostly amorphous with nanocrystallites.

Quantitative EDS data shows that the ion-damaged surface of the LF/LF He^+-irradiated olivine sample exhibits significant chemical differences compared to the bulk, unaltered olivine material. Segregation of Mg and Si is observed within ~30-65 nm of the surface (Fig. 6D, 6E, and S4). Within this zone, Mg and Si segregate into either roughly rounded pockets or more laterally elongated lenses oriented approximately parallel to the sample surface (Fig. 6D, 6E, and S4). In many areas, the outermost ~5-20 nm of this segregation zone is enriched in Fe and depleted in Mg and Si. However, this thin, Fe-rich layer is not completely laterally continuous (Fig. 6D). Localized lenses of Fe-enrichment also can occur up to ~ 30 nm below the surface. Some areas deviate from these overall compositional trends, exhibiting a Si-rich, Fe-poor, and extremely Mg-depleted layer (5-25 nm thick) directly at the surface which is underlain by elongated layers of Mg and Si segregation that are consistent with other regions of the sample (Fig. S4). In this same compositionally unique region, Fe content is also elevated above bulk abundance within a ~ 55 nm region near the surface.

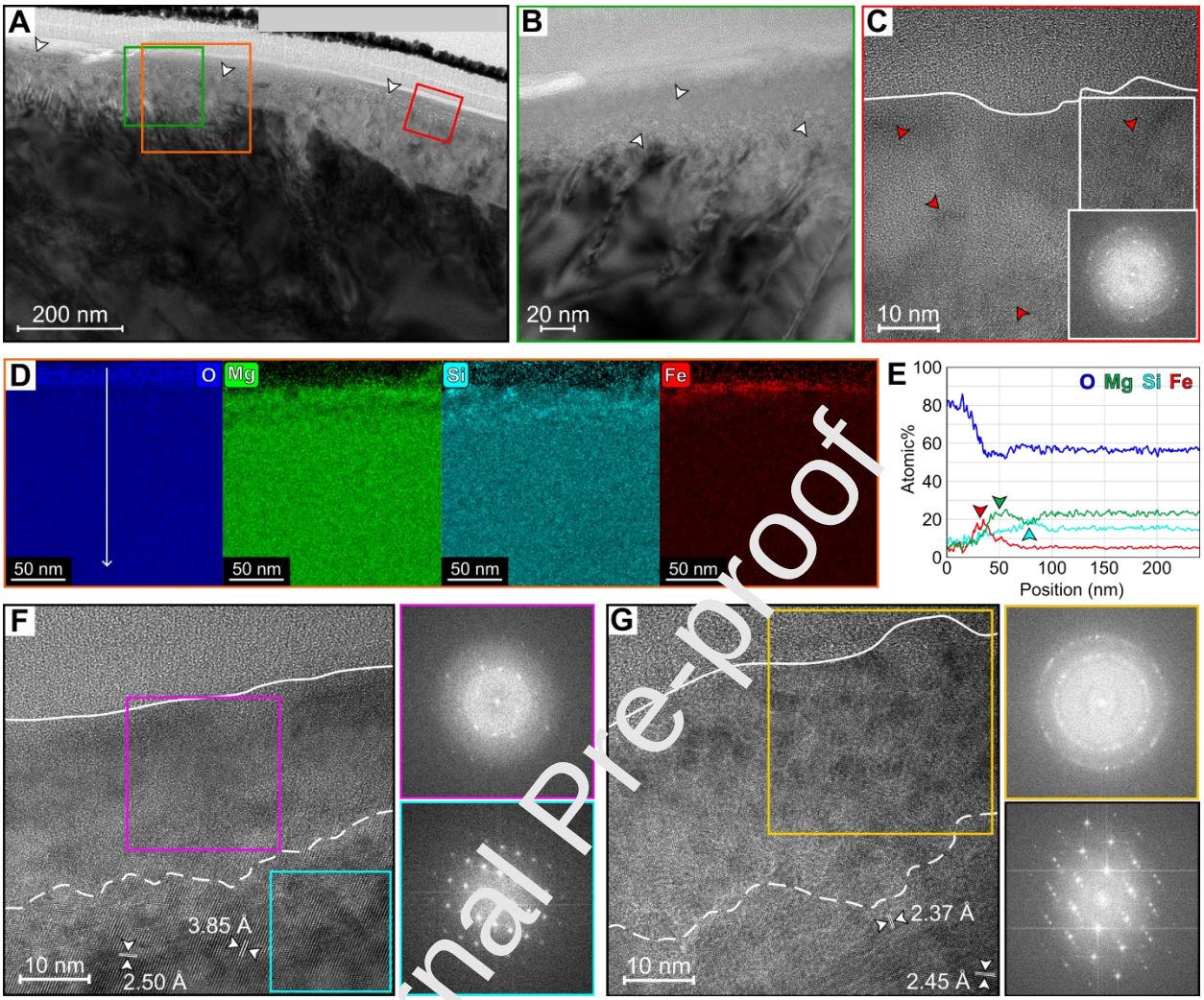

Figure 6. TEM imaging and microanalysis of the LF/LF He^{+}-irradiated olivine sample. (A) Conventional BF TEM mosaic showing the vesiculated ion-damaged surface and grain boundaries within the bulk sample. The white arrows indicate a couple vesicles larger than 10 nm in size. (B) Higher magnification conventional BF TEM image of the area indicated by the green box in (A). Some vesicles within the outermost ~40 nm of the sample are indicated by white arrows. These are less than 10 nm in size. (C) HRTEM image of the region indicated by the red box in (A) showing polycrystallinity (red arrows) and partial amorphization. Polycrystalline domains occur up to the surface of the olivine grain. The inset FFT was acquired from the white box and confirms nanocrystallinity at the surface. (D) Quantitative EDS map set of the region denoted by the orange box in (A). O is shown in blue, Mg, in green, Si in cyan, and Fe in red. The outer ~45 nm of the sample exhibits segregation of Si and Mg into localized pockets or lenses. Within this segregation zone, the outer ~6-16 nm is Fe-enriched. (E) A quantified elemental concentration profile extracted from the white arrow in (D). Colored arrows indicate regions of relative enrichment in a particular element, with green corresponding to Mg, cyan to Si, and red to Fe. (F) HRTEM image of an area of the ion-damaged rim that exhibits significant partial amorphization. FFT callouts below indicate the microstructure of the partially amorphous ion-altered region (magenta outline) and the unaltered crystalline olivine substrate (cyan outline). Measured d-spacings of 3.85 Å and 2.50 Å are also indicated which correspond to

the {021} and {131} family of planes, respectively. (G) HRTEM image of a surface region with strong polycrystallinity, as indicated by the bottom left FFT (yellow outline). The black outlined FFT shows the microstructure of the unaltered crystalline substrate. Measured d-spacings of 2.45 Å and 2.37 Å are also indicated which correspond to the {112} and {041} family of planes, respectively. For all panels, solid white lines denote the surface of the sample and dashed white lines denote the boundary between the ion-damaged surface and unaltered olivine substrate.

3.3.2.2 High flux/low fluence (HF/LF) He^+-irradiated olivine. Similar to the LF/LF He^+-irradiated sample, the HF/LF He^+-irradiated sample contains vesicles that are spherical, ovoid, and oblong in shape, but vesicle density is higher, overall, in this sample. Most vesicles occur in a continuous band between ~15-45 nm below the surface across the entire sample (Fig. 7A and 7B). Vesicles in this band are ≤20 nm in size and larger sizes are more common compared to the LF/LF He^+-irradiated olivine FIB-section. There are also bubbles up to 40 nm in size beyond the vesiculated band, up to ~110 nm below the surface.

TEM imaging shows the presence of two microstructurally distinct layers in this sample. The outermost ~6-15 nm (Fig. 7A and 7B) forms a light contrast layer that is mostly amorphous and contains nanocrystallites (Fig. 7C and 7D). Following this outer layer is a more strongly nanocrystalline region (Fig. 7C and 7D) with comparably less amorphization. Partial amorphization occurs as either pockets or elongated domains. The boundary between the ion-altered nanocrystalline region and unaltered crystalline olivine is not consistently well-defined but, where this transition is identifiable, it occurs between 15-80 nm below the surface in thickness. Finally, in a few localized regions, the ion-damaged surface remains crystalline but exhibits high defect densities.

EDS analysis reveals three laterally continuous, compositionally distinct zones (Fig. 7E and 7F). Zone 1 occurs in the outermost 10-18 nm of the sample and is characterized by significant Mg enrichment (54 at %), while Si (2 at%) and O (44 at%) are depleted. Zone 1 roughly correlates with the partially amorphous, nanocrystallite-bearing surface layer observed in HRTEM imaging. Zone 2 varies considerably in thickness across the sample, ranging from 15-50 nm. Here, Mg content gradually increases (sometimes exceeding bulk Mg abundance) while Si and O content gradually decreases moving from the grain interior towards Zone 1. Zone 3 ranges in thickness from 40-80 nm and exhibits minor Si enrichment and Mg depletion, overall, with no observed change in O.

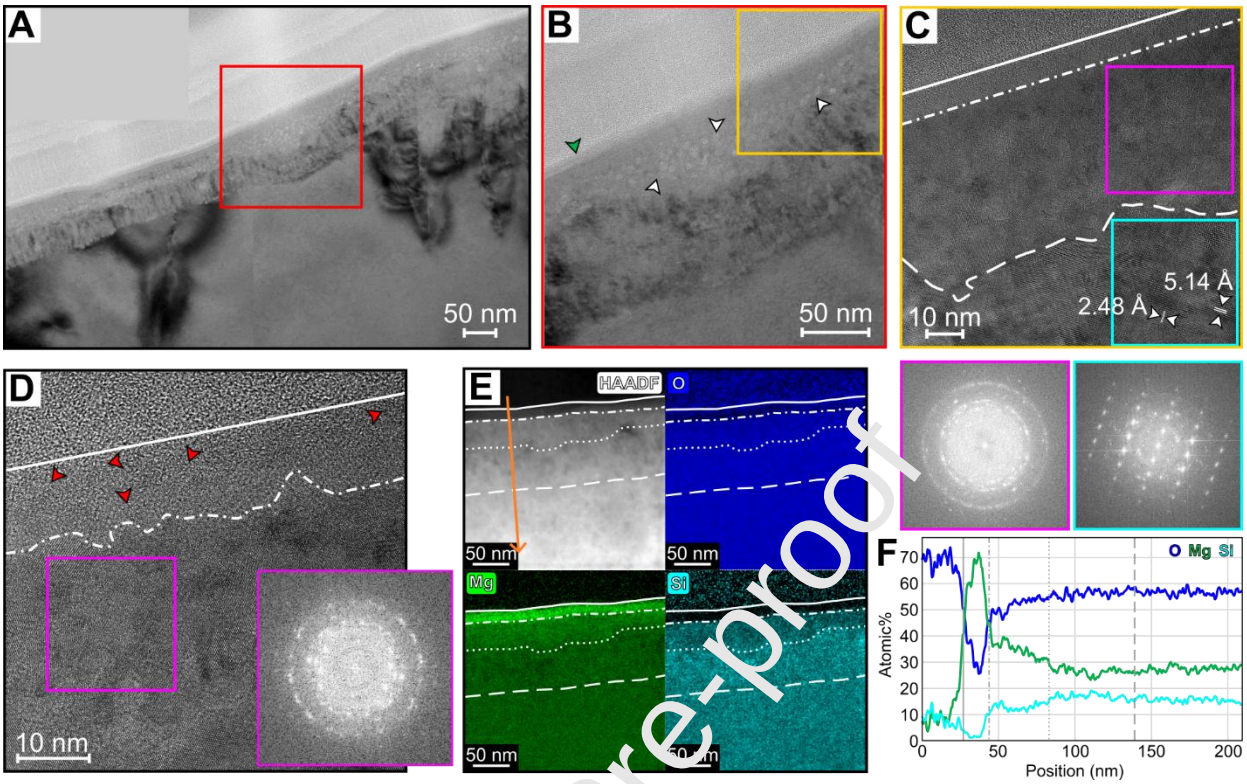

Figure 7. TEM and microanalysis of the LF/LF He^{+}-irradiated olivine sample. (A) Conventional BF TEM mosaic showing the vesiculated ion-irradiated surface of the sample. (B) Higher magnification BF TEM image of the area indicated by the red box in (A). White arrows denote vesicles and the green arrow denotes the thin light contrast surface layer. (C) HRTEM image of the strongly polycrystalline ion-altered region. The FFTs below confirm the polycrystalline microstructure of the surface (magenta outline) and the crystalline microstructure of the unaltered olivine substrate (cyan outline). The base of the ~10 nm light contrast surface layer is denoted by the dotted-dashed white line. Measured d-spacings of 5.14 Å and 2.48 Å are also indicated which correspond to the {011} and {112} family of planes, respectively. (D) A higher magnification HRTEM image highlighting the nanocrystalline (red arrows) and partially amorphous microstructure of the light contrast surface layer in the outermost ~10 nm of the sample. The inset FFT (magenta) shows that the remainder of the damaged rim is polycrystalline. (E) Quantitative EDS map set and its corresponding HAADF image with O in blue, Mg in green, and Si in cyan. The three compositionally distinct zones are shown. The base of zone 1 is denoted by the dotted-dashed white line, the base of zone 2 is denoted by the dotted white line and the base of zone 3 is denoted by the dashed white line. (F) A quantified elemental concentration profile extracted from the gray arrow in (E). The boundaries of zones 1, 2 and 3, are indicated in this graph. For all panels, solid white lines indicate the surface of the sample.

3.3.3 H^{+}-irradiated and He^{+}-irradiated matrix samples

The ion irradiated matrix samples analyzed in this study exhibit many similarities in microstructure and composition, and, thus, we discuss their characteristics together. The matrix samples lack well-defined, highly vesiculated ion-altered surface layers (Fig. 8-10). The LF/LF

H^+-irradiated FIB-section and HF/LF H^+-irradiated FIB-section are most similar to each other. Vesicles are randomly distributed at or near the surface and their density is very low. The maximum vesicle sizes in the LF/LF H^+-irradiated sample and HF/LF H^+-irradiated sample are 30 nm and 50 nm, respectively. It should be noted that discriminating between vesicles and inherent microporosity was sometimes difficult. Surface microstructures range from partially amorphous and nanocrystalline to mostly amorphous with weak nanocrystallinity. The degree of partial amorphization varies laterally and distinct lattice fringes with d-spacings indicative of serpentine-group phyllosilicates (~7 Å) are observed near the surface in both samples: within 12 nm of the surface for the LF/LF H^+-irradiated sample and within 20 nm of the surface for the HF/LF H^+-irradiated sample.

The surfaces of the LF/LF and HF/LF He^+-irradiated matrix samples exhibit distinct differences compared to the H^+-irradiated matrix samples analyzed in this study (Fig. 10 and 11). Vesiculation is more abundant in both samples, however, this texture occurs more continuously across the surface in the HF/LF He^+-irradiated sample (Fig. 10A, 11A). In the LF/LF He^+-irradiated sample, vesicles tend to form more localized clusters (Fig. 10). Most vesicles in both samples range from 3-35 nm in size, with some reaching up to ~75 nm. Compared to the vesiculated surface texture observed in the He^+-irradiated matrix cross-section from Laczniak et al. (2021), which experienced a higher total fluence (~10^{16} ions/cm^2), this sample exhibits a smaller vesicle size, vesicle density, and vesiculated layer thickness. Microstructurally, the surfaces of these matrix samples are predominantly amorphous. FFT images do show faint reflections indicating there is some nanocrystallinity in the ion-damaged regions (Fig. 10B, 11B, and 11D). Although the boundary between the ion-damaged surface and substrate matrix material is usually not well-defined in these samples, some localized regions of the HF/LF He^+-irradiated olivine FIB-section show a more defined ion-altered zone which typically measures between ~50-60 nm (Fig. 11A). We also observed distinct phyllosilicate lattice fringes in HRTEM images at depths as shallow as ~30 nm in both He^+-irradiated samples. Overall, the LF/LF and HF/HF He^+-irradiated FIB sections exhibit more extensive amorphization than the H^+-irradiated matrix samples analyzed here.

Similar to other reports of Murchison mineralogy, EDS analysis suggests that all matrix FIB-sections from this study consist mostly of fine-grained Mg- and Fe-bearing phyllosilicates and tochilinite with inclusions of magnetite, sulfides, pyroxene, and olivine (e.g., Barber, 1981; Tomeoka and Buseck, 1985; Zolensky et al., 1993; Bland et al., 2004). Their surfaces are dominated by O, Fe, Si, and Mg with smaller amounts of Al, P, Na, and/or S (≤2 at%). In all matrix samples, no difference between the chemical composition of the ion-irradiated region and underlying matrix material is observed.

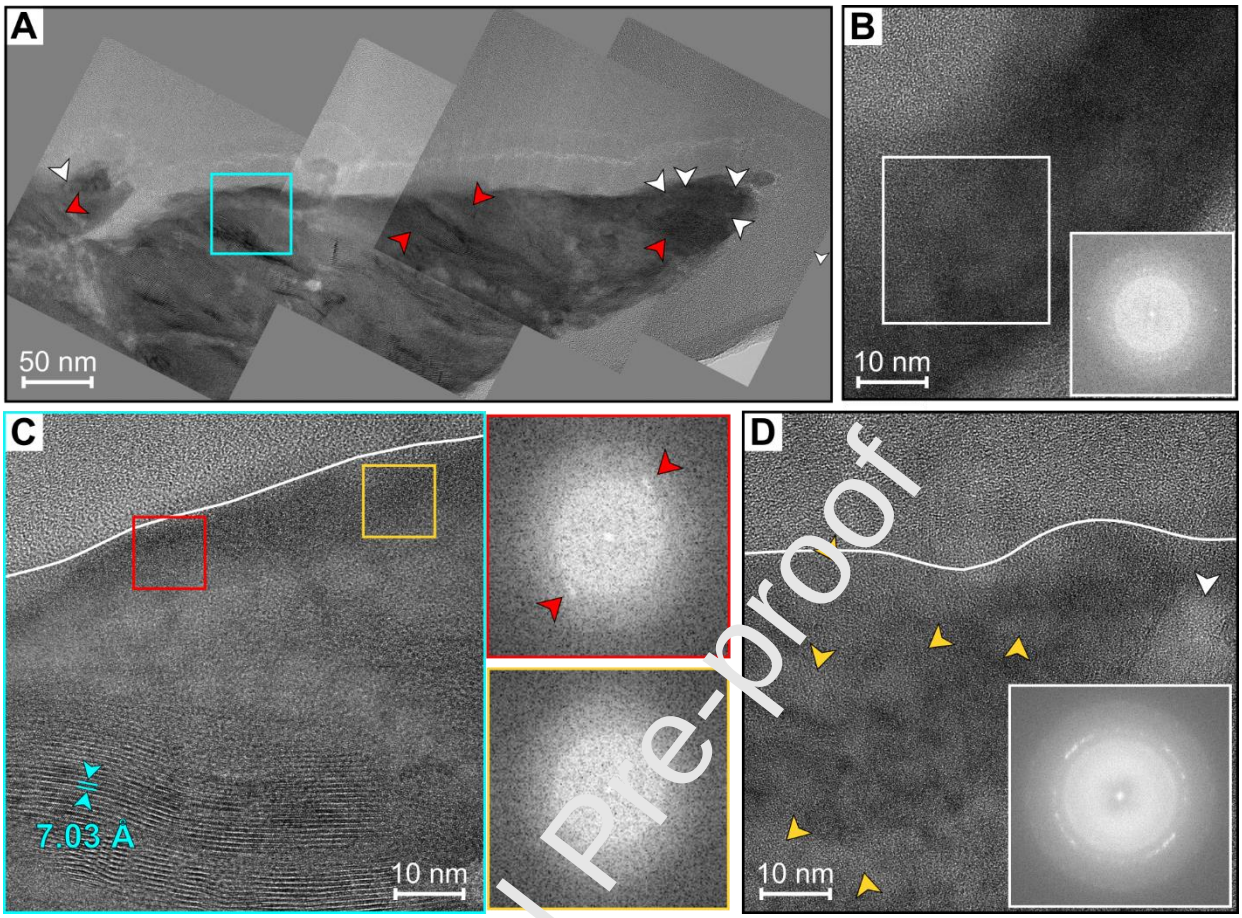

Figure 8. TEM and microanalysis of the LF/LF H^+-irradiated matrix sample. (A) Conventional BF TEM mosaic showing the presence of phyllosilicate lattice fringes near the surface of the sample. Red arrows indicate crystalline phyllosilicates near the surface. White arrows indicate possible vesicles. (B) HRTEM image of an area that is predominantly amorphous with weak crystallinity. Inset FFT is from the white box. (C) HRTEM image of the area indicated by the cyan box in (A) showing distinct phyllosilicate lattice fringes occurring just ~15-20 nm below the surface. Inset FFTs show that either nanocrystalline (red box) or amorphous (yellow box) material occurs directly at the surface of the sample. (D) HRTEM region showing a region that is partially amorphous with greater nanocrystallinity. Yellow arrows indicate amorphous pockets. The white arrow denotes a possible vesicle cluster.

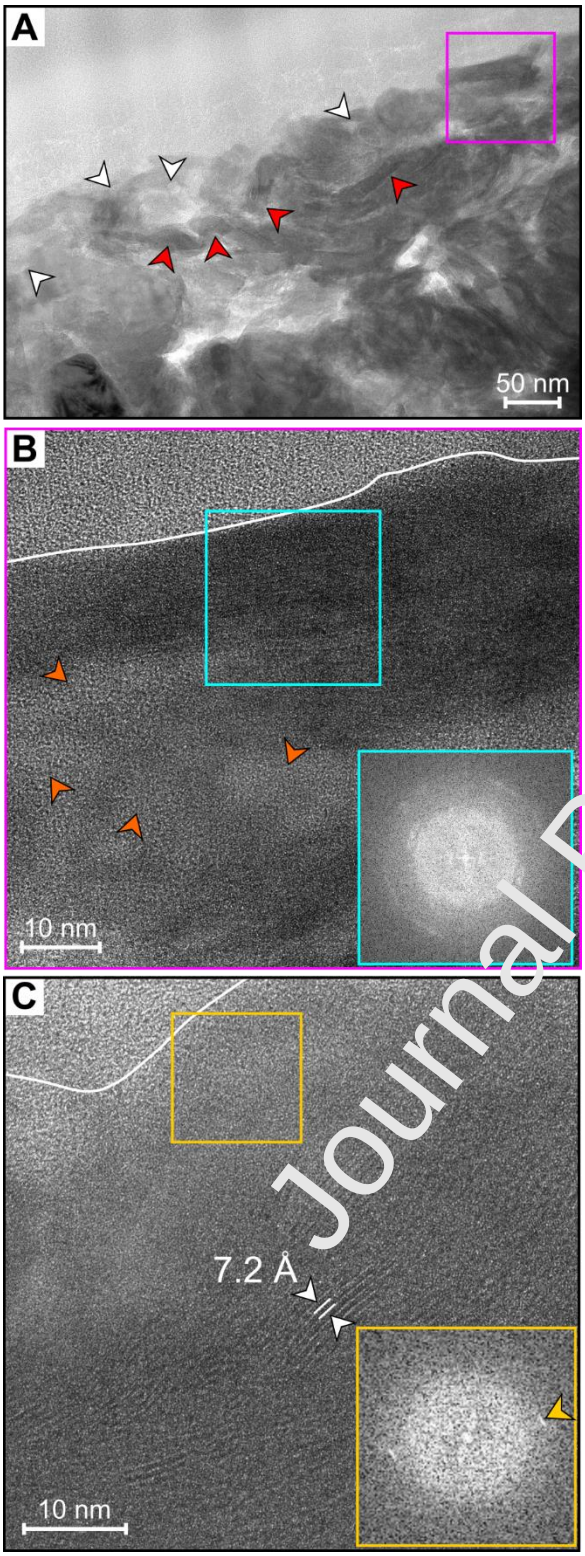

Figure 9. TEM and microanalysis of the HF/LF H^+-irradiated matrix sample. (A) BF TEM image of the ion irradiated surface of the sample. Note the lack of a distinct, noticeable altered surface layer. White arrows indicate possible vesicles. Red arrows denote some regions with visible lattice fringes consistent with serpentine phyllosilicates. (B) HRTEM image of the area denoted by the magenta box in (A). The surface is characterized by partial amorphization (orange arrows). The inset FFT (cyan) shows that some regions maintain crystallinity at the uppermost surface of the sample. (C) HRTEM image of a different area showing some crystalline phyllosilicates ~20 nm below the surface. The inset FFT shows that the layer above the phyllosilicates is weakly crystalline. In panels (B) and (C), the white line defines the surface of the sample.

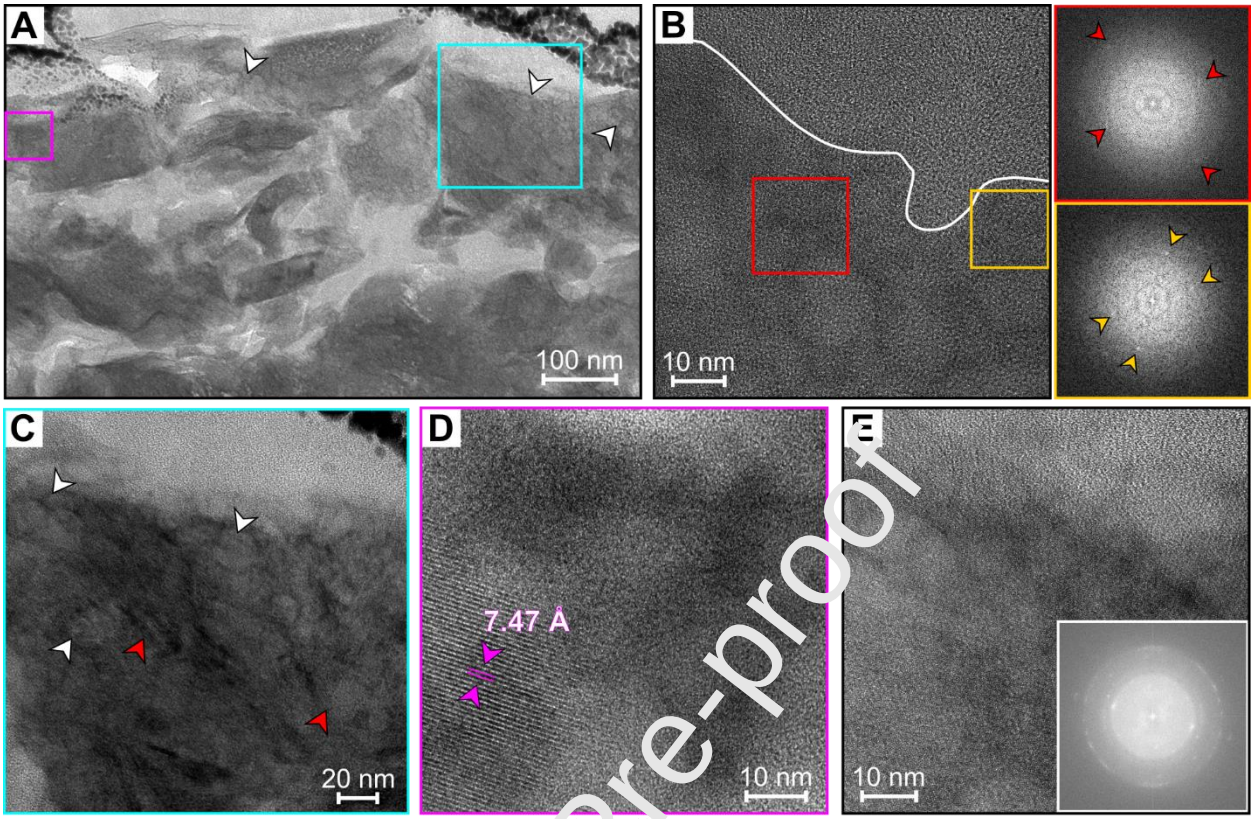

Figure 10. TEM and microanalysis of the HF/LF He^{+}-irradiated matrix sample. (A) BF TEM image of the ion irradiated surface of the sample. White arrows indicate clusters of vesicles. (B) HRTEM image of an area exhibiting weak crystallinity at the surface. Faint reflections are visible in the FFTS at right. (C) Higher magnification image of the region denoted by the cyan box in (A). White arrows point to vesicles. Red arrows denote some regions containing lattice fringes consistent with serpentine phyllosilicates. (D) HRTEM image of the region indicated by the magenta box in (A) showing lattice fringes consistent with chrysotile ~40 nm below the surface of the sample. (E) HRTEM image of a surface area exhibiting greater nanocrystallinity. FFT is inset at bottom right. In panel (B), the white line defines the surface of the sample.

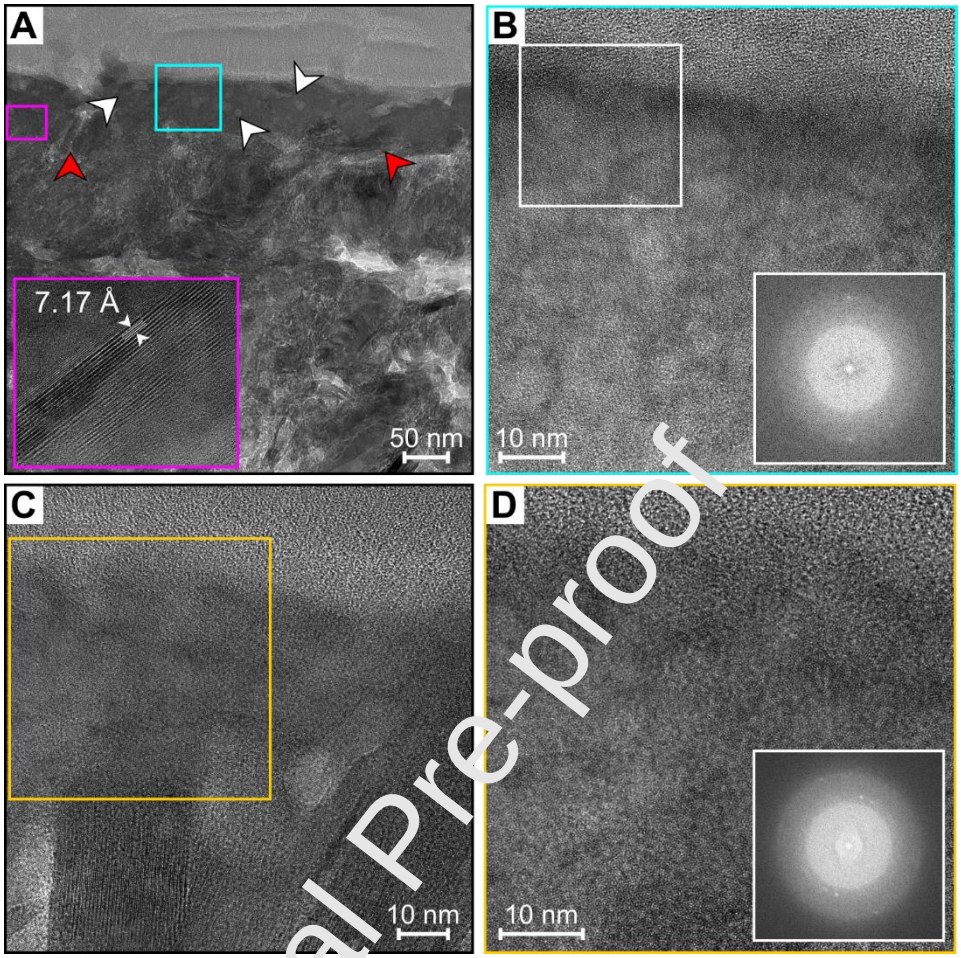

Figure 11. TEM imaging of the TF/LF He^{+}-irradiated matrix sample. (A) Conventional BF TEM image showing a region of the ion-damaged surface that resembles the smooth layers observed in Ryugu regolith grains. White arrows indicate vesicles and red arrows indicate visible phyllosilicate lattice fringes. The inset HRTEM image was acquired from the region outlined in magenta and shows phyllosilicate lattice fringes occurring ~55 nm below the surface. The 7.17 Å d-spacing is consistent with serpentine. (B) HRTEM image acquired from the area outlined by the cyan box in (A) showing that nanocrystallinity occurs directly at the surface of the sample. (C) HRTEM image showing a transition from the ion-altered surface to unaltered crystalline phyllosilicates. (B) A higher magnification HRTEM image acquired from the yellow box in (C) showing the weakly crystalline microstructure of the ion-damaged layer.

Table 2. Summary of TEM and EDS results from the eight FIB-sections analyzed in this study as well as those analyzed by Laczniak et al. (2021). Unless otherwise noted, descriptions start at the outer surface of the sample and move towards the sample interior. Arrows indicate transitions into deeper layers. Note that the abbreviation "HF/HF" used in the Laczniak et al. (2021) FIB-section names stands for high flux/high fluence.

FIB-Section	Thickness	Vesiculation Description	Microstructure	Surface Chemistry
This Study				
LF/LF H^+-irradiated olivine	30-60 nm*	Possible nanovesicles (2-5 nm) and elongated defects	*Variable:* (a) crystalline and highly strained; (b) nanocrystalline and partially amorphous with some zones where original olivine microstructure is maintained	Continuous Mg-enriched, Si-depleted, and slightly O-depleted layer (~10 nm) → segregation of Mg and Si into pockets or elongated lenses + slight overall O enrichment (up to 80 nm)
HF/LF H^+-irradiated olivine	~30 nm	Possible nanovesicles (2-5 nm) and elongated defects	Discontinuous light-contrast, partially amorphous layer (≤5 nm) → crystalline but highly strained	*Variable:* (a) Discontinuous Si-depleted and slightly Mg- and Fe-enriched layer (5-10 nm) → gradual increase in O an decrease in Mg with an Fe-poor band roughly in the center of the layer (35-45 nm); (b) No change
LF/LF He^+-irradiated olivine	20-65 nm*	Localized vesicles ≤15 nm in size between 10-35 nm from the surface	Localized and discontinuous light-contrast layer that is mostly amorphous with nanocrystallites (~7-10 nm) → partial amorphization and varying degrees of nanocrystallinity	*Variable:* Discontinuous Fe-enriched, Mg- and Si-depleted layer (5-20 nm) **OR** discontinuous Si-enriched, Fe- and Mg-depleted layer (5-25 nm) → segregation of Mg and Si into pockets or elongated lenses with localized lenses of Fe enrichment (30-65 nm)
HF/LF He^+-irradiated olivine	15-80 nm*	Band of vesicles ≤20 nm in size between 15-45 nm from the surface	*Variable:* (a) continuous light-contrast layer that is mostly amorphous with nanocrystallites	Mg-enriched, Si- and O-depleted layer (10-18 nm) → gradual increase in Mg and decrease in Si and O content (15-50

		with larger vesicles scattered at greater depths	(~6-15 nm) → strongly nanocrystalline and partially amorphous layer; (b) crystalline but highly strained	nm) → minor Si enrichment and Mg depletion (40-80 nm)
LF/LF H^+-irradiated matrix	Not well-defined	Not abundant and randomly distributed	*Variable:* Partially amorphous and nanocrystalline **OR** mostly amorphous with weak nanocrystallinity	No change
HF/LF H^+-irradiated matrix	Not well-defined	Not abundant and randomly distributed	*Variable:* Partially amorphous and nanocrystalline **OR** mostly amorphous with weak nanocrystallinity	No change
LF/LF He^+-irradiated matrix	Not well-defined	More abundant and forms more localized clusters (3-35 nm in size)	Predominantly amorphous with weak nanocrystallinity	No change
HF/LF He^+-irradiated matrix	50-60 nm when well-defined	More abundant and laterally continuous (3-35 nm in size)	Predominantly amorphous with weak nanocrystallinity	No change
Laczniak et al. (2021) *– "HF/HF" is an abbreviation for high flux/high fluence*				
HF/HF H^+-irradiated Mg-rich olivine	50-85 nm	Moderate abundance	Partially amorphous to completely polycrystalline (lateral variation)	Variable; Some regions have a thin laterally discontinuous Si-enriched/Mg-depleted layer → Mg-enriched/Si-depleted layer (~20-30 nm); Refer to paper for more descriptions
HF/HF H^+-irradiated	~65 nm	Low abundance	Partially amorphous → completely amorphous → partially amorphous	Mg- & Fe-enriched/Si-depleted layer (2-5 nm) → discontinuous Si-enriched/Mg-

Fe-rich olivine				& Fe-depleted layer (~10-20 nm) → Si content progressively increases toward base of ion-affected region
HF/HF He^+-irradiated Mg-rich olivine	~75 nm	Moderate abundance	Completely amorphous layer (uppermost ~15 nm) → partially amorphous layer	Si-enriched/ Mg-depleted layer (upper 20-40 nm)
HF/HF He^+-irradiated Fe-rich olivine	120-180 nm	High abundance	Completely amorphous	No change
HF/HF H^+-irradiated matrix	~65 nm	High abundance	Completely amorphous	No change
HF/HF He^+-irradiated matrix	~150 nm	High abundance	Completely amorphous	No change

* The boundary between the ion-damaged surface and unaltered substrate was not consistently well defined

4. Discussion

Ion irradiation experiments performed in this study modified the spectral characteristics, microstructure, and composition of the Murchison meteorite. Here we discuss the relationship between these modifications and incident ion flux as well as the implications of our results in the context of other experimental solar wind simulations and returned sample analyses.

4.1 Optical changes

Slope bluing is observed in the LF/LF H^+-irradiated, HF/LF H^+-irradiated, and HF/LF He^+-irradiated spectra in this study and is primarily driven by brightening in the lower wavelength region. This same trend has been recognized in previous ion irradiation experiments with natural hydrocarbons in which the alteration was attributed to the carbonization and dehydrogenation process (Moroz et al., 2004). These processes involve the loss of oxygen- and hydrogen-bearing organic functional groups and the rearrangement of carbon atoms into large aromatic clusters with short-range order (Lantz et al., 2017; Moroz et al., 2004). Optically, ion irradiation-induced carbonization and dehydrogenation decreases the optical gap of complex organics, imbues semi-metallic properties in the material, and increases the material's absorption coefficient in the visible wavelength range. The corresponding increase in optical density causes surface scattering to dominate reflectance, and, as a result, brightening occurs in the visible wavelength region (Jones, 2012; Lantz et al., 2017; Moroz et al., 2004). We believe carbonization of Murchison's organic component may be contributing to the slope bluing of this study's HF/LF H^+- and He^+-irradiated spectra and LF/LF H^+-irradiated spectrum. Carbonization and dehydrogenation of organic material was also invoked to explain the bluing trend observed in CM and CI carbonaceous chondrites irradiated with 40 keV He ions up to a fluence on the same order of magnitude used in our experiments (Lantz et al., 2017), and it is thought to be one process that might be occurring on asteroid Bennu (DellaGiustina et al., 2020; Simon et al., 2020). Our experiments suggest that carbonization and dehydrogenation by solar wind space weathering can occur on relatively short timescales and, thus, corroborate findings from analyses of VNIR data acquired by the OSIRIS-REx mission, which indicate that rapid breakdown of aliphatic and aromatic organic species may be occurring on Bennu's surface ($<10^4$ years) (Kaplan et al., 2021).

XPS results from both the LF/LF and HF/LF fluence experiments also support carbonization and dehydrogenation as a mechanism for spectral change. Although our XPS data show that only a small amount of carbon is removed from the sample's surface (<12 at%), the ~286.2 eV (C-O-C) and ~288.6 eV (O-C=O) peaks associated with organic functional groups disappear from high-resolution XPS spectra, even after low fluence irradiation. The disappearance of these peaks represents a loss of O, and thus, indicates that carbonization may be occurring in response to ion irradiation. The carbonization/dehydrogenation process is further supported by the minor reduction in O content that is observed in some LF/LF survey XPS spectra. However, the increase in

There is no evidence for surface reduction of Fe to metallic Fe in our XPS data, suggesting that metallic Fe nanoparticles are not forming or contributing to the spectral signature at this stage. Increased microroughness derived from ion irradiation is also known to cause brightening, as diffuse reflection is greater than specular reflection on rougher surfaces (Moroz et al., 2004; Thompson et al., 2020, 2019b). However, the wavelength dependent brightening seen

in reflectance spectra presented here suggests that microroughness is likely only one of several possible contributing factors.

We also note that the LF/LF H^+- and He^+-irradiated spectra exhibit higher albedo across all wavelengths compared to the unirradiated spectrum, with the H^+-irradiated spectrum showing greater overall brightening. This difference likely arises from variation in the abundance of chondrules or differences in surface roughness between the Murchison slabs. Chondrules exhibit higher albedo across the entire VNIR wavelength range compared to matrix material, and rougher surfaces result in greater reflectance due to higher diffuse reflection, as discussed above (Dukes et al., 2015; Matsuoka et al., 2020; Moroz et al., 2004; Thompson et al., 2020, 2019b; Vernazza et al., 2013). Sputtering and removal of opaque carbon species also may cause spectral brightening across the full VNIR range (e.g., Cloutis et al., 2011a, 2011b; Dukes et al., 2015; Hendrix et al., 2016). However, because XPS results show only a small reduction in overall carbon content, this process likely plays only a minor role in the observed brightening trend. Effects from compositional heterogeneity, surface roughness, carbon removal, and carbonization/dehydrogenation are likely all simultaneously changing the spectral signature of our samples.

Because both studies used incident ion fluxes of the order of ~10^{13} ions/cm^2/s, by comparing unirradiated and irradiated spectra from our HF/LF irradiated samples to VNIR results from Laczniak et al. (2021), we can evaluate spectral effects that could be related to increasing simulated exposure time. Experiments performed by Laczniak et al. (2021) also irradiated Murchison slabs with 1 keV H^+ and 4 keV He^+, but the fluences employed in those experiments were ~1.5-2.0 orders of magnitude higher than those used in this study and, thus, represent a longer solar wind exposure time compared to the experiments here. The canonical model of space weathering based on anhydrous planetary regoliths drives spectra to darken and redden over time. In this work, HF/LF H^+ and He^+ irradiated VNIR spectra exhibit slightly bluer slopes compared to the unirradiated Murchison spectra. Our LF/LF H^+-irradiated spectrum is also bluer than its unirradiated counterpart. This contrasts with spectral trends from Laczniak et al. (2021) which showed minor brightening longward of ~0.65 µm, and, thus, overall slope reddening, in response to high flux/high fluence H^+ and He^+ irradiation. Our results show that samples may experience early bluing until ultimately exhibiting spectral reddening with continued irradiation exposure, suggesting that solar wind irradiation alone could induce multi-stage space weathering on carbonaceous asteroidal regoliths. Multi-stage space weathering also was observed in VNIR spectra of laser irradiated Murchison samples whereby initial laser irradiation caused darkening and subsequent laser irradiation caused brightening (Thompson et al., 2020), further confirming the complexity of space weathering on carbonaceous regoliths.

Interestingly, the fluence dependent transition from bluing to reddening discussed above resembles color variation trends observed on the surface of asteroid Bennu. Multispectral images of Bennu suggest that fresh, unaltered regolith exhibits a redder spectral slope than the average spectral signature of Bennu's surface. The initial stages of space weathering cause brightening in the near-ultraviolet wavelength region, yielding a blue overall slope, similar to the bluing observed in our HF/LF experiments. With continued exposure, brightening occurs in the visible and near-infrared range, neutralizing the slope (DellaGiustina et al., 2020). This finding, in conjunction with experimental space weathering studies (e.g., this study; Lantz et al., 2017; Thompson et al., 2020; Laczniak et al., 2021), provides evidence that non-linear, multi-stage space weathering may be typical of some C-complex asteroid surfaces. Numerous physiochemical processes with conflicting spectral trends, such as carbonization, surface

roughness, mineralogical diversity, carbon removal, and more, are likely occurring concurrently and contributing to the overall spectral signature of our Murchison sample and primitive, carbonaceous asteroidal regoliths in outer space.

4.2 Microstructural alteration

4.2.1 Vesiculation

Vesiculation has become a characteristic feature of space weathering in both returned samples and experimental analogs. Some ferromagnesian silicate grains returned from asteroid Itokawa contain lenticular or oblong vesicles in their outermost ~50 nm which are oriented roughly parallel to the sample surface and form "blistered" surface textures (e.g., Matsumoto et al., 2014, 2015b; Noguchi et al., 2014b; Thompson et al., 2014; Burgess and Stroud, 2021). Although vesicles are common to lunar agglutinates, vesiculated textures are comparatively rare in space weathered rims of lunar soil grains–especially in solar wind-damaged rims–even though their exposure times are typically orders of magnitude *larger* than Itokawa samples (Keller and McKay, 1997, 1993; Noble et al., 2005; Thompson et al., 2016, 2014). However, a few recent investigations revealed the presence of a variety of vesicle morphologies near the surface of a few space weathered lunar soil particles, including irregular, lenticular, rounded, flat, and linear shapes (Cymes et al., 2023; Kling et al., 2023). Additionally, vesicles <50 nm in diameter have recently been identified in the smooth surface layers of phyllosilicate-rich regions of Ryugu grains (Noguchi et al., 2022). Although ion implantation is known to cause vesiculation, other processes and conditions besides solar wind irradiation, such as heating effects from nearby micrometeoroid impacts, might contribute to the formation and/or destruction of vesicles (e.g., Keller and McKay, 1993, 1997; Brownlee et al., 1998; Noble et al., 2005; Thompson et al., 2014, 2017, 2020; Laczniak and Thompson, 2023). To further complicate our understanding of vesiculation, ion-damaged regions of experimentally irradiated minerals and meteorite samples often exhibit vesicle densities that *exceed* returned sample observations (e.g., Demyk et al., 2001; Carrez et al., 2002; Christoffersen et al., 2010; Gillis-Davis et al., 2017; Laczniak et al., 2021; Chaves and Thompson, 2022). Collectively, these findings suggest that the role of space weathering on vesicle development and cycling is poorly understood.

Previous investigators have suggested that incident ion flux affects bubble formation in lunar samples (Tamhane and Agrawal, 1979). Under low flux conditions, volume diffusion more effectively reduces the concentration of implanted H and He within a given area. As such, a higher critical fluence is required for saturation to occur and vesicles to form (Tamhane and Agrawal, 1979). This means, if two samples were irradiated up to the same total fluence, we would expect to see less vesiculation and smaller vesicles in the sample irradiated with a lower incident ion flux compared to the sample irradiated with a higher incident flux. Results from our experiments provide *limited* support for a flux-dependence on vesicle formation. While both the LF/LF and HF/LF He^+-irradiated olivine samples contain vesicles, vesiculated textures are more continuous and vesicle density is higher in our HF/LF He^+-irradiated olivine. Additionally, in our HF/LF He^+-irradiated olivine sample, isolated vesicles are distributed sporadically at depths between ~75-110 nm and the largest measured vesicles occur in this region. These findings may be attributed to the higher flux used during He^+ irradiation of this sample. We also note that the presence of spherical, oblong, and ovoid vesicles in the ion-altered surface of this study's LF/LF He^+-irradiated olivine sample contrasts with experimental results from a He^+-irradiated olivine

from Matsumoto et al. (2015a). Although it was irradiated with a flux and fluence approximately one order of magnitude *higher* than the experimental conditions used in our study (a flux of 1×10^{12} ions/cm^2/s and fluence of 3×10^{17} ions/cm^2), the surface of that olivine grain exhibited only "precursor" vesicles rather than spherical or ovoid vesicles. Crystallographic orientation and/or differences in olivine composition may have contributed to this discrepancy between our study and that of Matsumoto et al. (2015a).

The LF/LF and HF/LF H^+-irradiated olivine samples from this study exhibit interesting vesiculated textures. The ion-altered surfaces of both samples contain small (~2-5 nm), roughly spherical features that appear light in contrast in BF TEM images which could be interpreted as nanovesicles. The density of these features is greater in the HF/LF H^+-irradiated olivine, which may reflect a flux effect. The ion-damaged rims of our LF/LF and HF/LF H^+-irradiated olivine samples also contain elongated light-contrast features oriented sub-parallel to the sample's surface which are reminiscent of "precursor" or "collapsed" vesicles in solar-wind damaged rims of ferromagnesian Itokawa silicates and experimentally irradiated olivine grains. Authors suggest that "precursor" vesicles in returned samples and experimental analogs represent zones where implanted ions have begun to accumulate (T. Matsumoto et al. 2015; Toru Matsumoto et al., 2015; Noguchi et al., 2014b). Similar elongated cavities (or "platelets") also were identified in spinel grains irradiated with high energy H and He beams (0.4 and 0.8 MeV, respectively). These platelets were interpreted to be two-dimensional clusters of vacancies and interstitial H and He ions which represent the early stages of three-dimensional vesicle development (Zinkle, 2012a). Considering the relatively low irradiation fluences achieved in our experiments, the elongated features observed in our samples also may signify the incipient stages of vesiculation induced by H^+-irradiation.

Overall, the LF/LF and HF/LF He^+-irradiated matrix and olivine samples from this study exhibit greater vesiculation than the LF/LF and HF/LF H^+-irradiated matrix and olivine samples, indicating that He may be more efficient at forming vesicles in olivine and phyllosilicate-rich materials than H. In support of this, Zinkle (2012) found that critical vesiculation fluences were higher for H^+ irradiation than He^+ irradiation in many ceramic materials. As a result, He implantation may largely control vesicle formation in relatively immature/submature returned samples from airless bodies. Further studies examining solid-state diffusion of implanted H and He could confirm this finding.

4.2.2 Crystallinity

Prolonged ion irradiation introduces structural defects into crystalline materials by way of atomic displacements. Complete amorphization of a material can occur when the defect density (i.e., atomic displacements) within a crystal structure reaches a critical threshold, but this threshold can depend on both the irradiation conditions as well as the intrinsic factors of a material's crystal structure (e.g., bonding, crystal chemistry). Depending on the material and irradiation conditions it is also possible that dynamic recovery processes may counteract defect accumulation such that the material maintains crystallinity even to extremely high irradiation fluences. Laboratory simulations suggest that olivine has a critical amorphization fluence between 1 to 5×10^{16} ions/cm^2 when irradiated with 4 keV He^+ (using a beam density of 9 μA/cm^2) (Carrez et al., 2002). However, solar-wind damaged rims of returned olivine particles are predominantly crystalline in microstructure even though their exposure timescales exceed this critical amorphization fluence. Ion flux has been proposed as a possible explanation for the

microstructural discrepancy between naturally and experimentally irradiated olivine grain surfaces because the solar wind has a flux approximately 4-5 orders of magnitude lower than ion fluxes used in laboratory space weathering simulations (Burgess and Stroud, 2021; Harries and Langenhorst, 2014; Keller et al., 2016; Keller and Berger, 2014; Keller and McKay, 1997, 1993; Noguchi et al., 2014b, 2011; Thompson et al., 2014). Under the significantly lower flux of solar wind, damage from ion implantation accumulates more slowly, which may allow the olivine crystal structure to avoid amorphization by removing or dynamically rearranging point defects into more energetically stable configurations (e.g., Claverie et al., 1991; Haynes and Holland, 1991; Wirth, 2007; Christoffersen et al., 2020; Keller et al., 2021).

Interestingly, results from this study do not indicate a strong flux dependence on the degree of amorphization or lattice damage in olivine. All samples in this study were irradiated to total fluences within or above the critical fluence range required for amorphization of olivine, but no evidence of complete amorphization was observed within the surfaces of the He^+- or H^+-irradiated olivine grains. In fact, the olivine irradiated to the highest overall fluence and with higher ion flux–the HF/LF H^+-irradiated olivine FIB-section exhibited the *least* lattice damage overall. More specifically, the surface microstructure of the HF/LF H^+-irradiated olivine sample is predominantly crystalline, but highly strained, and appears very similar to the solar-wind damaged rims of returned lunar and Itokawa ferromagnesian silicates (Burgess and Stroud, 2021; Harries and Langenhorst, 2014; Keller et al., 2016; Keller and Berger, 2014; Keller and McKay, 1997, 1993; Noguchi et al., 2014b, 2011; Thompson et al., 2014). The critical amorphization fluence for olivine irradiated with 1 keV H^+ is not yet known. Therefore, it is possible that neither of the two H^+ irradiation experiments performed in the present study reached total fluences needed for complete amorphization of olivine. However, the fact that TEM imaging from this study demonstrates that the ion-altered region of the HF/LF H^+-irradiated olivine sample maintains more of its original crystal structure than its LF/LF fluence counterpart is quite interesting, especially since it received a higher irradiation dose. We also observe a surprising microstructural difference in our He^+-irradiated olivine FIB-sections. The LF/LF He^+-irradiated olivine grain exhibits surface regions where amorphous material dominates over nanocrystalline material whereas the surface of the HF/LF He^+-irradiated olivine sample is consistently dominated by nanocrystalline or crystalline domains rather than amorphous material. This is the opposite trend one would expect from an ion flux effect. We do note that HF/LF He^+-irradiated olivine exhibits a laterally continuous, thin light contrast outer layer marked by amorphization and nanocrystallinity while such a layer is highly localized and discontinuous in the LF/LF He^+-irradiated olivine sample. The continuous, more well-developed nature of this outer layer in the HF/LF He-irradiated olivine may relate to the higher experimental ion flux.

Collectively, the microstructural results discussed above suggest that, at the total fluences employed in this study, incident ion flux may not be the *only or primary* variable controlling the crystalline-amorphous transition of olivine. Crystallographic orientation is another variable that also likely influences lattice damage in olivine. Li et al. (2013) showed that aligning the incident 50 keV He^+ beam such that implantation occurred parallel to the [010] zone axis resulted in more efficient degradation of the crystal structure. Planes perpendicular or near-perpendicular to [010]–particularly (040)–were amorphized more quickly and easily than planes approximately parallel to [100] or [001] due to a higher atomic density along [010] direction. Irradiation experiments on enstatite grains also revealed a similar orientation-dependence on amorphization efficiency (Schrempel et al., 2002). The idea that crystallographic orientation affects amorphization of olivine is supported further by the lateral variation in surface microstructure

observed in our LF/LF H^+-irradiated, LF/LF He^+-irradiated, and HF/LF He^+-irradiated olivine FIB-sections, all of which exhibit grains boundaries. In these samples, some regions of their ion-altered surface maintain much of the original olivine structure while others exhibit partial amorphization and nanocrystallinity. In returned samples, the combined effects of crystallographic orientation and the extremely low flux of natural solar wind–which is approximately three orders of magnitude *lower* than the low ion fluxes employed in this study–may account for the lack of complete amorphization of olivine grains. We also note that other variables such as olivine Mg content, surface roughness and shadowing effects, and pre-existing substrate deformation may also contribute to the microstructural trends observed here and in returned regoliths (e.g., Wang and Ewing, 1992; Wang et al., 1993; Laczniak et al., 2021). Future studies investigating the relationship between crystallographic orientation and lattice damage by solar wind relevant ions are important for understanding the crystalline-amorphous transition of minerals common to airless bodies and have implications for models that predict surface exposure timescales from solar-wind damaged rims.

In the case of the matrix FIB-sections, microstructural damage is similar in the LF/LF and HF/LF H^+-irradiated FIB-sections. Alternatively, unlike the LF/LF He^+-irradiated matrix FIB-section, the HF/LF He^+-irradiated matrix sample exhibits regions with a more defined, uniformly thick, laterally extensive, and predominantly amorphous ion-altered zone. Considering both He^+-irradiated samples received nearly identical total fluences, this may reflect an ion flux effect. Additionally, these more defined ion-damaged regions in our HF/LF He^+-irradiated matrix sample closely resemble the smooth solar-wind damaged layers identified in space-weathered Ryugu regolith grains which also exhibit nearly complete amorphization (but can reach up to ~100 nm in thickness) (Noguchi et al., 2022). This similarity provides further evidence that smooth layers on Ryugu grains were most likely formed by solar wind irradiation and may indicate that He plays a more significant role than H in forming these layers. Solar flare track measurements from one Ryugu olivine particle suggest that an exposure time greater than ~3,000 years is required to form noticeable 20 nm-thick smooth layers on phyllosilicate-rich Ryugu regolith grains (Noguchi et al., 2022). Interestingly, this study's HF/LF He^+ irradiation experiment, which corresponds to a simulated exposure time of only ~400 years, produces mostly amorphous matrix surface layers that tend to be ~50-60 nm in thickness when well defined. This comparison between exposure time and Ryugu matrix "rim" thickness versus our experimentally irradiated matrix sample may suggest that, under the low flux conditions of the solar wind, it may take longer to form recognizable ion damaged layers in phyllosilicates.

4.3 Chemical alteration

No significant compositional difference between the ion-altered surface and original matrix material is observed in any of our matrix FIB-sections. This finding is consistent with previous ion irradiation experiments and results from laboratory analyses of smooth, solar wind-damaged layers in returned Ryugu particles (Laczniak et al., 2021; Noguchi et al., 2022). Although the elemental compositions in our study's matrix FIB-sections remain unchanged, XPS analyses suggest a minor chemical reduction of Fe^{3+} to Fe^{2+} with ion irradiation, creating a slightly more reduced surface region. Electron energy-loss spectroscopy (EELS) and X-ray absorption near-edge spectroscopy (XANES) analyses have revealed a similar trend in Ryugu grains, with smooth space weathered layers showing an enrichment in Fe^{2+} relative to Fe^{3+} (Noguchi et al., 2022). XPS analyses from Laczniak et al. (2021) also revealed the reduction of

Fe^{3+} to Fe^{2+} with progressive irradiation, and a small portion of metallic Fe was observed at experiment completion. Reduction to metallic iron was *not* observed in this study's XPS spectra, which likely reflects the lower total fluences (i.e., lower simulated exposure times) used in our experiments.

Unlike the matrix samples, the ion-damaged surfaces of olivine FIB-sections are compositionally distinct from the unaltered bulk mineral, and chemical changes observed within a single FIB-section can vary across its surface. Overall, the chemical alterations derived from ion irradiation in this study are complex, and likely are formed by multiple processes acting contemporaneously. Below, we identify similarities and differences between the compositional changes in our olivine samples and explain the variety of ion irradiation processes that are likely contributing to the formation of the complicated compositional trends that we observe.

Although this layer is not laterally continuous in every sample, all olivine samples have some version of an outermost, comparatively thin layer that is chemically distinct from the remainder of the ion-affected surface. In the LF/LF H^+-irradiated olivine (Fig. 4D-4E, S3) and HF/LF He^+-irradiated olivine (Fig. 7B-7F), this layer *is* laterally continuous and is characterized by Mg enrichment above bulk olivine content and Si and O depletion. In both samples, these layers are nanocrystalline with amorphous material. Interestingly, XPS spectra from the LF/LF H^+ irradiation experiment show a decrease in O abundance with progressive ion irradiation, which aligns with the O depletion observed in the outer layer of the LF/LF H^+-irradiated olivine grain. In comparison, XPS results from the HF/LF He^+ irradiation experiment revealed a decrease in O content in only *some* analyzed locations. Alternatively, in the HF/LF H^+-irradiated olivine (Fig. 5B-5F) and LF/LF He^+-irradiated olivine (Fig. 6D-6E, S4), the chemically distinct outer layer is more localized. The HF/LF H^+-irradiated outer layer is slightly enriched in Mg and Fe and depleted in Si and exhibits partial amorphization only. Discontinuous surface layers with similar compositions has been observed in some Itokawa pyroxene and olivine grains and H^+-irradiated Murchison olivine (Chaves and Thompson, 2022; Laczniak et al., 2021; Noguchi et al., 2014b, 2014a; Thompson et al., 2019). Finally, the localized outer layer of the LF/LF He^+-irradiated olivine sample is marked by Fe enrichment and Mg and Si depletion and may correspond to microstructural surface domains of partial amorphization and nanocrystallinity.

In returned samples and experimentally ion irradiated analogs, sputtering is often presented as one possible mechanism contributing to the formation of thin surface layers with compositions that deviate non-stoichiometrically from the underlying host mineral. Surface layers of both returned Itokawa samples and experimentally irradiated minerals have been attributed to preferential sputtering (e.g., Keller and McKay, 1997; Dukes et al., 1999; Carrez et al., 2002; Noguchi et al., 2014b). However, the chemical enrichments and depletions produced by sputtering of ferromagnesium silicates can be somewhat difficult to predict, largely due to the fact that preferentially sputtering is controlled by a variety of factors including atomic mass, surface binding energy, and elemental abundances of the target material (Johnson, 1989; Wehner, 1959). Based on atomic mass alone, one would expect the lighter elements in olivine, Mg and O, to be preferentially sputtered over Si and Fe. The high relative concentration of O in olivine may also promote preferential sputtering of the element. Sputtering derived depletions in O and Mg were previously identified at the surface of olivines irradiated with H^+ and He^+ (e.g., Bradley et al., 1996; Demyk et al., 2001; Carrez et al., 2002). Preferential sputtering of O may contribute to O-depletion observed in the outer layers of the LF/LF H^+-irradiated and HF/LF He^+-irradiated olivine samples while sputter redeposition may contribute to the Mg-enrichment observed in the same layer. However, Si and/or Fe are not completely absent in these layers, so

other processes are likely at play. Additionally, preferential sputtering and redeposition alters target chemistry only up to depths of ~10 nm, and, thus, other processes are required to explain the thickness of some of these outer layers.

The minor reduction in C content revealed by XPS analyses of all irradiation Murchison samples most likely reflects sputtering and removal of both intrinsic and contaminant carbon species. Although this change in C content does not appear to be dependent on ion flux, we do observe a fluence dependence. The degree of C depletion in our experiments is small compared to the significant depletion observed in H^+ and He^+ irradiation experiments from Laczniak et al. (2021), suggesting that that longer fluences, and, thus, longer exposure times, lead to a greater decreases in C abundance.

Another dominant trend observed in three of the four ion irradiated olivine samples (i.e., the LF/LF H^+-irradiated olivine (Fig. 4D, S3), the LF/LF He^+-irradiated olivine (Fig. 6D, S4), and the HF/LF He^+-irradiated olivine (Fig.7E)) is the segregation of Mg and Si within the bulk of the ion-damaged region. In more Fe-rich olivines, the Fe tends to segregate with Mg. This segregation occurs in three types of morphologies: pockets, elongated lenses parallel to the sample surface, and laterally continuous layers. Interestingly, ion flux may affect the morphology of Mg-Si segregation in our He^+-irradiated olivine samples. In the LF/LF He^+-irradiated olivine, elemental partitioning occurs as either pockets (Fig. 6D) or elongated lenses (Fig. S4) while the HF/LF He^+-irradiated olivine contains distinct, laterally continuous, and thicker layers of Mg enrichment and Si depletion and vice versa (Fig. 7E). The higher flux of He^+ may promote faster chemical alteration, allowing formation of defined layers rather than isolated lenses. It is important to note that Carrez et al. (2001) observed segregation of Mg and Si in their San Carlos olivine samples after prolonged exposure to a 300 keV electron beam. More explicitly, they observed the formation of periclase (or ferropericlase) nanocrystallites within an amorphous SiO_2 phase after reaching a total fluence of $3x10^{20}$ e^-/cm^2 due to radiolysis effects. Therefore, we must consider the possibility that electron beam damage during EDS analysis could have caused some degree of Mg and Si segregation in our samples. However, in some regions, we see elongated lenses or layers of Mg or Si enrichment/depletion rather than discrete, roughly spherical nanocrystallites. Due to the more laterally continuous nature of these zones, processes other than beam damage likely contribute to the chemical segregation.

Compositional heterogeneity observed in our olivine FIB-sections, including both Mg-Si segregation and the formation of the thin outer layers, is likely driven, at least in part, by radiation enhanced diffusion (RED) and radiation induced segregation (RIS). These processes rely on the accumulation of high concentrations of point defects in the crystal lattice from ion irradiation. In RED, defect accumulation accelerates the migration of mobile defects along chemical potential gradients, such as those produced by preferential sputtering or recoil implantation, to try to reach an equilibrium state (e.g., Ho, 1978; Sigmund, 1981; Cheng et al., 1992; Wang et al., 2004). As a result, RED can effectively widen chemically altered layers, and has been invoked to explain compositional heterogeneity in space weathered lunar ilmenite and Itokawa olivine grains as well as ion irradiated olivine (Chaves and Thompson, 2022; Christoffersen et al., 1996; Laczniak et al., 2021). In this study's samples, RED may increase the thickness of the Fe- or Mg-rich outer layers beyond what is possible through just preferential sputtering. Crystallographic orientation, temperature, atom mobility, and degree of lattice damage are all variables that impact the rate of RED in a material (e.g., Buening and Buseck, 1973; Ho, 1978; Sigmund, 1981; Hermeling and Schmalzried, 1984; Cheng et al., 1992; Chakraborty et al., 1994; Dohmen et al., 2002; Wang et al., 2004). The crystallographic

orientation effect, in particular, may help explain the variation in chemical trends observed within the same olivine FIB-section.

In radiation induced segregation (RIS), certain constituent atomic species are preferentially attracted to point defects produced by irradiation. This solute-defect coupling effect causes atomic transport either towards or away from defect sinks (e.g., grain boundaries, dislocations, and voids), creating relative compositional enrichments and depletions near these sites (Nastar and Soisson, 2012; Zinkle, 2012b). In some cases, the extent of enrichment and depletion is significant enough that new phases precipitate. Noguchi et al. (2014b) offered RIS as a possible mechanism for the formation of $npFe^0$ particles within the predominantly crystalline solar wind-damaged rims of Itokawa olivine and pyroxene grains. It is likely that RIS plays some role in the partitioning of Mg and Si within the ion-damaged surfaces of our olivine samples. Although RED and RIS are well-studied in metal targets, investigations aimed at understanding how these processes affect ferromagnesian silicates may significantly improve models of space weathering.

Recoil implantation is yet another process known to change the composition of ion irradiated materials whereby atomic collisions cause target atoms to be knocked out of their original lattice positions and implanted deeper within the sample. The mass of constituent atoms heavily influences the efficiency of recoil implantation with lighter elements being knocked into to deeper regions of the sample compared to heavier elements, yielding an enrichment in the lighter element at depth and an enrichment in the heavier element nearer the surface (Gailliard, 1984; Kelly and Sanders, 1976; Sigmund, 1981, 1979). If only recoil implantation was occurring, one would expect Si to concentrate near the surface of an olivine grain with Mg and O concentrating at depth, but this chemical trend is not universally observed in this study's olivine FIB-sections. In fact, Mg-enrichment tends to occur (at least occasionally) in three of our olivine samples. Although this does not necessarily discount recoil implantation as a mechanism for compositional alteration in our samples, it may play a relatively minor role compared to other processes.

4.4 Where is the nanophase Fe^0?

The formation of $npFe^0$ is a characteristic space weathering feature observed in returned samples and experimental analogs. Although other nanoparticle mineralogies have been identified in lunar and Itokawa grains, such as Fe sulfides and Fe oxides, $npFe^0$ is still abundant in melt and vapor deposits as well as solar-wind damaged rims of these samples (Burgess and Stroud, 2021; Harries and Langenhorst, 2014; Keller et al., 2016; Keller and Berger, 2014; Keller and McKay, 1997, 1993; Noguchi et al., 2014b, 2011; Thompson et al., 2014). Interestingly, recent laboratory analyses of returned Ryugu grains revealed very low abundances of $npFe^0$; Fe- and Fe-Ni-sulfides rather than metallic Fe vastly dominate the nanoparticle mineralogy (Matsumoto et al., 2022; Melendez et al., 2023; Noguchi et al., 2022; Thompson et al., 2022). Similar to the Ryugu samples, we did not confidently observe the formation of $npFe^0$– or nanoparticles of any mineralogy–in our samples. XPS spectra from this study, which show a reduction of Fe^{3+} to Fe^{2+} but not Fe^0, as well as the lack of slope reddening in our ion irradiated VNIR spectra also support the absence of $npFe^0$ particles. Collectively, these findings are consistent with the hypothesis that reduction to metallic Fe in materials with abundant Fe^{3+}-bearing phyllosilicates is difficult to accomplish with space weathering processes, especially through solar ion irradiation (Noguchi et al., 2022). While production of $npFe^0$ in phyllosilicate

matrix may not be expected, previous experimental simulations of solar wind irradiation suggest that $npFe^0$ should form in Fe^{2+}-bearing olivine bombarded by 1 keV H^+ and 4 keV He^+ ions (e.g., Dukes et al., 1999; Carrez et al., 2002). However, we did not identify $npFe^0$ in our olivine FIB-sections and neither did Laczniak et al. (2021). This absence of $npFe^0$ may indicate solar wind irradiation alone is not efficient at forming nanoparticles and that some thermal contribution, possibly from micrometeoroid impacts, is needed (e.g., Hood and Schubert, 1980; Kramer et al., 2011; Glotch et al., 2015).

5. Conclusion

To examine if differences in incident ion flux impact the spectral, microstructural, and chemical alteration of minerals common to carbonaceous asteroidal regoliths and better understand space weathering of C-complex asteroids, we performed a set of low flux and high flux H^+ (1 keV) and He^+ (4 keV) irradiation experiments on small slabs of the Murchison CM2 meteorite. Both sets of experiments were irradiated to similar total fluences (between ~3×10^{16} to ~6×10^{16} ions/cm^2) but used different ion fluxes: ~10^{11} ions/cm^2/s for the low flux experiments and ~10^{13} ions/cm^2/s for the high flux experiments. Using XPS, VNIR, and TEM, we analyzed the spectral, microstructural, and compositional changes induced by these ion irradiation experiments. XPS analyses show that both low flux and high flux H and He irradiation cause minor depletion in surface carbon content and the chemical reduction of iron from Fe^{3+} to Fe^{2+} without the formation of metallic iron. Considering we also did not identify $npFe^0$–or any Fe-bearing nanoparticles–in olivine and matrix cross-sections analyzed with TEM, $npFe^0$ may be an uncommon space weathering product in carbon-rich asteroidal regoliths containing abundant ferric iron bearing minerals. Although we do not observe a flux effect in this study's VNIR results, reflectance spectra of the LF/LF H^+-irradiated slab and LF/LF and HF/LF He^+-irradiated slabs are slightly bluer in slope compared to unirradiated Murchison which may reflect carbonization of organic material.

Microstructural analyses with TEM did not reveal a strong flux-dependence on the crystalline-amorphous transition of olivine. A variety of microstructures were observed in olivine ion-damaged surfaces, however, no zones of complete amorphization were observed. We hypothesize that crystallographic orientation plays a role in the amorphization efficiency of olivine in this study. Paired with the extremely low flux of natural solar wind, crystallographic orientation effects may significantly contribute to the lack of completely amorphous solar wind damaged rims in returned olivine samples. Additional ion irradiation investigations examining the effect of crystallographic orientation on amorphization are needed to further understand solar wind space weathering of ferromagnesian silicates. TEM analysis of matrix samples suggest that He irradiation may primarily drive surface alteration of phyllosilicates with higher ion fluxes promoting the development of more well-defined ion-damaged rims, similar to the smooth layers found in returned Ryugu grains. Furthermore, our results also provide *some* evidence that higher ion fluxes lead to greater vesiculation and that He is more effective at vesicle formation. Although matrix surface regions do not differ in composition compared to unaltered material at depth, olivine surfaces exhibit complex chemical changes. Higher ion fluxes appear to promote the formation of more laterally continuous lenses or layers of Mg and Si segregation in olivine. These complicated trends are likely driven by a combination of processes occurring

simultaneously including sputtering, sputter redeposition, radiation enhanced diffusion, radiation induced segregation, and recoil implantation. Based on this study, solar wind-damaged rims in returned regolith grains from asteroid Bennu may lack npFe^0 as well as other Fe-bearing nanoparticle mineralogies. Phyllosilicate-rich regions could exhibit nearly or completely amorphous ion-altered rims with minor vesiculation and no change in composition compared to the bulk particle. Rims in ferromagnesian silicates may show a range of microstructures from predominantly crystalline to partially amorphous with nanocrystalline domains, and some degree of Mg and Si segregation may be observed. Overall, findings from this work corroborate the complexity of space weathering of carbonaceous asteroidal regoliths.

6. Acknowledgements

This research was supported by the following sources of funding: (1) NSF MRI award #1626201, which allowed the University of Virginia Nanoscale Materials Characterization Facility to purchase the Versaprobe III XPS instrument used in this study; (2) NASA Solar System Workings grant 80NSSC19K0960; (3) Future Investigators in NASA Earth and Space Science and Technology award 80NSSC21K1534; and (4) the Johnson Space Center Coordinated Analysis Work Package funded by the NASA Internal Scientist Funding Model. We thank M. Zolensky and the Arizona State University Buseck Center for Meteorite Studies (BCMS) for providing the Murchison samples used in this study (BCMS catalog # 828) and Z. Rahman for assisting with preparation of thin foils for TEM analysis. We also acknowledge the staff of the Purdue University Electron Microscopy Facility and the NASA Johnson Space Center Electron Beam Analysis Labs.

Supplementary Materials:

Investigating the role of incident ion flux in solar wind space weathering of carbon-rich asteroidal regolith via H^+ and He^+ irradiation of the Murchison meteorite

Table S1. Atomic concentrations measured with XPS before and after the LF/LF H^+ and He^+ irradiation experiments. The amount of increase or decrease in atomic concentration and percent change are also listed for each analyzed XPS point. The average analytical error for each elemental difference is as follows: C (±0.81), O (±0.70), Na (±0.07), Mg (±0.24), Al (±0.35), Si (±0.17), S (±0.07), Ca (±0.11), Fe (±0.07), Ni (±0.07). These errors, which are derived from the average standard deviation across all XPS analysis points, are applicable to all four irradiation experiments.

		C1s	O1s	Na1s	Mg2p	Al2p	Si2p	S2p	Cl2p	Ar2p	Ca2s	Fe3p	Ni2p3
LOW FLUX / LOW FLUENCE H^+ IRRADIATION													
Point 1 (Inclusion)	Before	23.2	57.3	0.2	3.4	1.2	8.1	0.5	0.0	0.4	0.8	4.4	0.6
	After	19.3	56.3	0.6	4.5	1.6	9.6	[illegible]	0.0	0.7	0.1	6.7	0.6
	Increase/decrease	-3.8	-0.9	0.3	1.1	0.4	1.5	-0.5	0.0	0.2	-0.7	2.3	0.0
	% change	-16.5	-1.6	161.9	33.2	30.6	[illegible]	-100.0	n/a	54.5	-87.7	53.7	6.9
Point 2 (Matrix)	Before	21.0	59.1	0.2	2.9	2.0	[illegible]	1.1	0.0	0.5	0.0	5.5	0.4
	After	18.7	55.8	0.6	2.9	2.6	8.7	1.5	0.0	0.7	0.0	8.5	0.2
	Increase/decrease	-2.3	-3.3	0.3	0.0	0.7	1.4	0.4	0.0	0.2	0.0	3.0	-0.2
	% change	-11.0	-5.6	129.2	-1.4	[illegible]	18.6	36.1	n/a	38.8	n/a	53.3	-44.2
Point 3 (Matrix)	Before	20.4	60.6	0.1	2.7	[illegible]	7.7	0.7	0.0	0.5	0.7	4.9	0.4
	After	17.2	56.0	0.0	3.8	2.7	8.8	1.1	0.0	0.6	0.7	8.1	1.0
	Increase/decrease	-3.2	-4.6	-0.1	[illegible]	[illegible]	1.1	0.4	0.0	0.0	0.0	3.2	0.7
	% change	-15.6	-7.5	-100.0	[illegible]	97.1	13.7	55.6	n/a	7.4	1.5	66.2	188.6
Point 4 (Matrix)	Before	20.9	59.6	0.2	[illegible]	0.9	8.4	0.9	0.0	0.6	0.0	5.0	0.5
	After	18.4	56.3	0.5	3.8	2.0	9.7	0.7	0.0	0.7	0.1	7.1	0.7
	Increase/decrease	-2.6	-3.2	0.3	0.7	1.1	1.4	-0.2	0.0	0.1	0.1	2.1	0.2
	% change	-12.2	-5.4	[illegible]	[illegible]	114.0	16.2	-17.4	n/a	15.0	n/a	41.1	53.3
Point 5 (Inclusion)	Before	19.5	60.5	[illegible]	3.6	0.6	8.0	1.2	0.0	0.5	0.7	4.6	0.4
	After	15.9	59.2	[illegible]	3.7	1.1	10.1	1.2	0.0	0.7	0.0	7.3	0.5
	Increase/decrease	-3.6	-1.3	0.0	0.1	0.5	2.1	0.0	0.0	0.1	-0.6	2.7	0.1
	% change	-18.5	[illegible]	4.3	1.7	82.0	26.8	-2.5	n/a	26.9	-95.5	57.1	23.1
LOW FLUX / LOW FLUENCE HE^+ IRRADIATION													
Point 1 (Inclusion)	Before	17.1	[illegible]	0.0	4.9	0.5	9.9	0.1	0.0	0.6	0.6	3.7	0.0
	After	12.2	59.7	1.0	6.1	1.1	12.2	0.7	0.3	0.9	0.4	5.0	0.4
	Increase/decrease	-4.9	-3.0	1.0	1.2	0.6	2.3	0.7	0.3	0.3	-0.2	1.3	0.4
	% change	[illegible]	-4.8	n/a	25.6	115.2	23.4	720.7	n/a	45.3	-29.1	34.0	n/a
Point 2 (Matrix)	Before	[illegible]	64.2	0.1	3.3	1.2	9.8	0.0	0.1	0.8	0.0	3.4	0.1
	After	8.7	66.4	0.4	4.6	1.2	11.9	0.0	0.0	1.3	0.0	5.5	0.0
	Increase/decrease	[illegible]	2.2	0.4	1.4	0.0	2.1	0.0	-0.1	0.5	0.0	2.0	0.0
	% change	-49.4	3.4	642.5	41.9	3.6	21.9	n/a	-90.6	64.1	n/a	59.2	-48.2
Point 3 (Matrix)	Before	16.6	60.8	0.6	5.0	0.9	9.9	1.4	0.2	0.7	0.0	4.0	0.0
	After	9.1	61.7	0.5	6.1	1.0	13.0	1.1	0.1	1.1	0.0	6.0	0.3
	Increase/decrease	-7.6	1.0	-0.1	1.1	0.1	3.1	-0.3	-0.1	0.4	0.0	2.0	0.3
	% change	-45.5	1.6	-12.0	22.8	15.1	31.3	-21.0	-58.6	62.9	n/a	48.9	n/a
Point 4 (Matrix)	Before	18.7	62.0	0.0	3.8	1.0	10.7	0.7	0.3	0.7	0.7	1.4	0.0
	After	11.9	61.9	0.7	4.7	1.3	14.0	0.9	0.1	0.9	0.9	3.0	0.0
	Increase/decrease	-6.9	-0.1	0.7	0.8	0.3	3.3	0.1	-0.2	0.2	0.2	1.6	0.0
	% change	-36.6	-0.2	6612.1	21.6	32.6	30.6	18.6	-68.0	34.6	31.9	112.5	n/a

Table S2. Atomic concentrations measured with XPS before and after the HF/LF H^+ and He^+ irradiation experiments. The amount of increase or decrease in atomic concentration and percent change are also listed for each analyzed XPS point. The average analytical error for each elemental difference is as follows: C (±0.81), O (±0.70), Na (±0.07), Mg (±0.24), Al (±0.35), Si (±0.17), S (±0.07), Ca (±0.11), Fe (±0.07), Ni (±0.07). These errors, which are derived from the average standard deviation across all XPS analysis points, are applicable to all four irradiation experiments.

		C1s	O1s	Na1s	Mg1s	Al2p	Si2p	S2p	Ca2s	Fe2p3	Ni2p3
HIGH FLUX / LOW FLUENCE H^+ IRRADIATION											
Point 1 (Matrix)	Before	18.9	59.2	0.9	5.7	1.0	7.8	1.7	0.2	4.4	0.1
	After	11.4	58.3	0.9	9.5	1.4	9.1	0.8	0.3	8.2	0.1
	Increase/decrease	-7.5	-0.9	0.0	3.8	0.4	1.2	-0.9	0.1	3.7	0.0
	% change	-39.5	-1.5	2.2	65.4	41.6	15.8	52.0	55.0	84.6	0.0
Point 2 (Inclusion)	Before	18.4	58.7	0.6	7.6	1.7	7.[illegible]	1.1	0.0	4.0	0.0
	After	15.9	59.5	0.4	8.9	1.5	8.2	0.5	0.0	5.1	0.0
	Increase/decrease	-2.5	0.8	-0.2	1.2	-0.2	0.4	-0.6	0.0	1.1	0.0
	% change	-13.6	1.4	-31.7	16.0	-10.5	5.3	-54.1	n/a	26.6	n/a
Point 3 (Matrix)	Before	18.9	59.2	0.7	5.9	1.1	7.3	1.8	0.5	4.4	0.2
	After	10.2	58.0	0.6	9.5	[illegible].1	9.5	1.2	0.7	8.2	0.1
	Increase/decrease	-8.7	-1.2	-0.1	3.6	[illegible].0	2.1	-0.6	0.2	3.7	-0.1
	% change	-46.1	-2.0	-12.9	60.0	[illegible]4.5	29.2	-32.6	42.0	84.4	-50.0
HIGH FLUX / LOW FLUENCE HE^+ IRRADIATION											
Point 1 (Matrix)	Before	18.0	59.4	0.6	6.[illegible]	1.6	7.9	1.0	0.4	4.5	0.2
	After	7.3	61.6	0.9	[illegible].0	1.6	10.0	0.5	0.6	7.4	0.2
	Increase/decrease	-10.8	2.2	0.3	3.[illegible]	0.0	2.2	-0.5	0.2	2.9	0.0
	% change	-59.6	3.7	51.7	55.5	0.6	27.6	-49.5	52.5	62.8	0.0
Point 2 (Inclusion)	Before	24.3	53.3	0.3	10.0	1.4	7.8	0.6	0.3	2.1	0.0
	After	16.2	53.9	0.3	16.2	1.3	8.8	0.1	0.5	2.7	0.0
	Increase/decrease	-8.1	0.6	0.[illegible]	6.2	-0.1	1.1	-0.5	0.2	0.6	0.0
	% change	-33.4	1.1	[illegible].[illegible]	62.1	-6.4	14.1	-83.3	70.0	29.9	n/a
Point 3 (Matrix)	Before	18.1	60.7	[illegible].7	4.8	1.3	8.1	1.2	0.1	4.9	0.1
	After	6.4	[illegible]1.4	0.9	10.4	1.8	10.0	1.0	0.6	7.4	0.1
	Increase/decrease	-11.7	0.[illegible]	0.2	5.6	0.5	2.0	-0.2	0.5	2.5	0.0
	% change	-64.8	1.2	30.0	115.7	38.9	24.5	-16.5	510.0	49.7	0.0

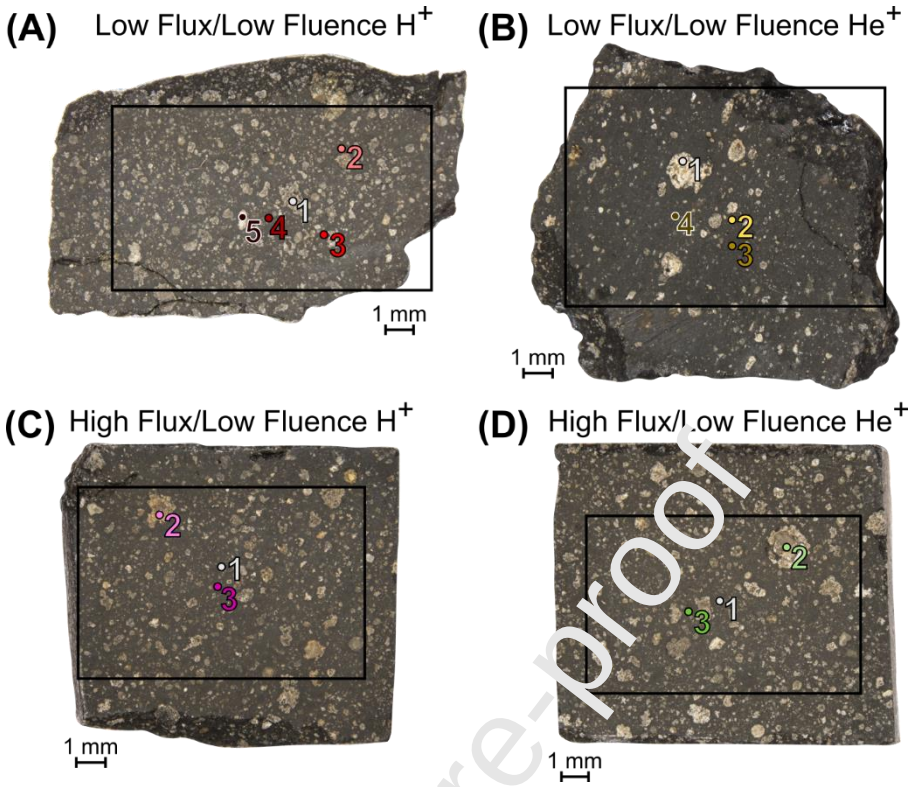

Figure S1. Locations from which XPS data were acquired during (A) low flux/low fluence (LF/LF) H^+ irradiation (B) low flux/low fluence (LF/LF) He^+ irradiation (C) high flux/low fluence (HF/LF) H^+ irradiation, and (D) high flux/low fluence (HF/LF) He^+ irradiation. The numbers associated with each analysis point correspond to those included in Tables S1 and S2. Black boxes indicate the area of ion irradiation.

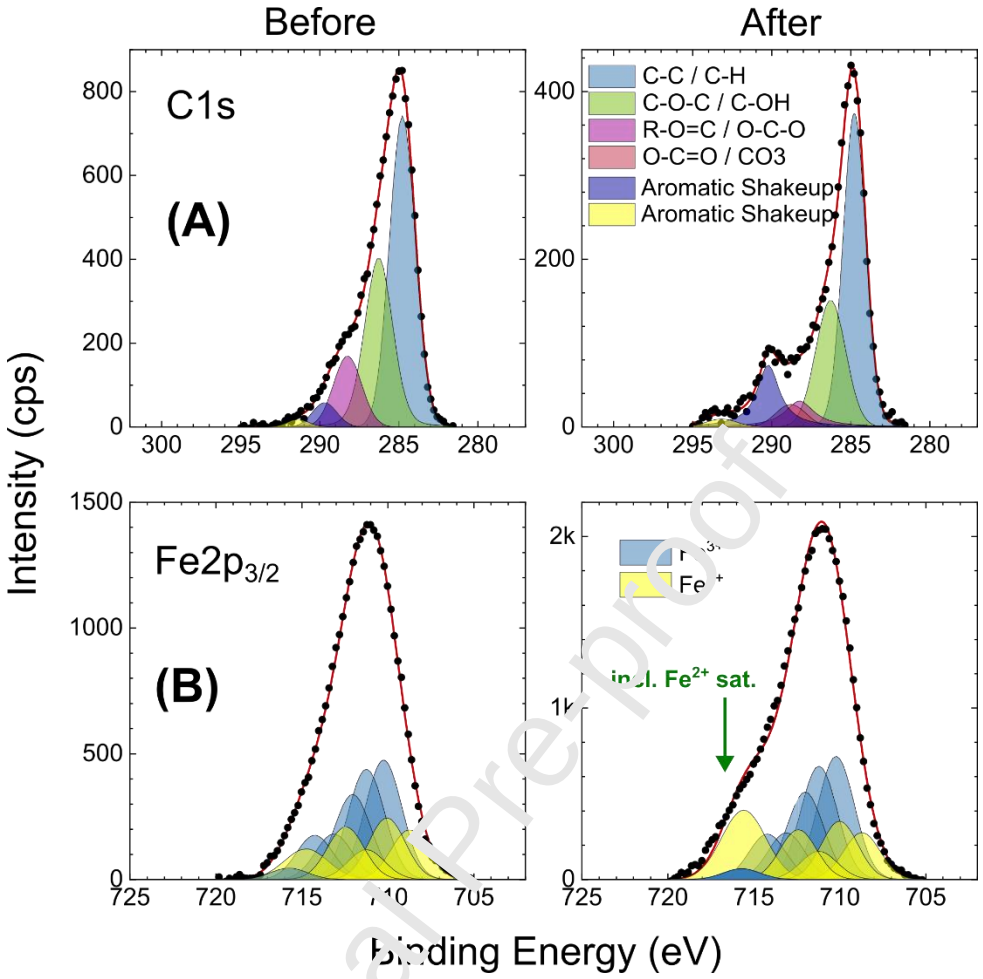

Figure S2. To extract detailed information about chemical changes under ion irradiation (H or He), high energy-resolution XPS spectra (pass energy = 26 eV) were collected as a function of ion fluence. Photoelectron peaks were subsequently fit, after Shirley background subtraction, with Gaussian-Lorentzian envelopes utilizing Multipak v.9.8. The full-width half maxima were initially required to be constant across each transition, varying between 1.0 and 1.6 eV, before removing constraints for the final fit. For Fe-2p features, where multiplet splitting is significant, we modeled our work after Biesinger et al. 2011. In this fitting example, we highlight chemical changes derived from high flux (9.1×10^{12} $He^+/cm^2/s$) 4 keV He^+ irradiation up to a total fluence of 2.0×10^{16} He^+/cm^2 (~400 years of exposure). "Before" spectra were acquired prior to irradiation while the "after" spectra were collected at 2.0×10^{16} He^+/cm^2. (A) 4 keV He^+ irradiation is observed to reduce the overall carbon content of Murchison, across all chemistries, particularly destroying carbonyl bonds and enhancing the aromatic hydrocarbon content, as noted by the enhancement of the two shakeup features at ~290 and ~293 eV. (B) Both Fe^{2+} and Fe^{3+} states are noted in the Fe-$2p_{3/2}$ spectra prior to irradiation, derived from magnetite, sulfide, olivine, and other phases, in addition to the formation of ferric iron on the Murchison surface from atmospheric exposure. With a fluence to 2.0×10^{16} He^+/cm^2, the Fe^{3+}: Fe^{2+} ratio is reduced slightly, and the formation of a Fe^{2+} satellite feature (shake up peak) due to final-state charge transfer is identified. All spectral binding energies are calibrated to C-H = 284.8 eV.

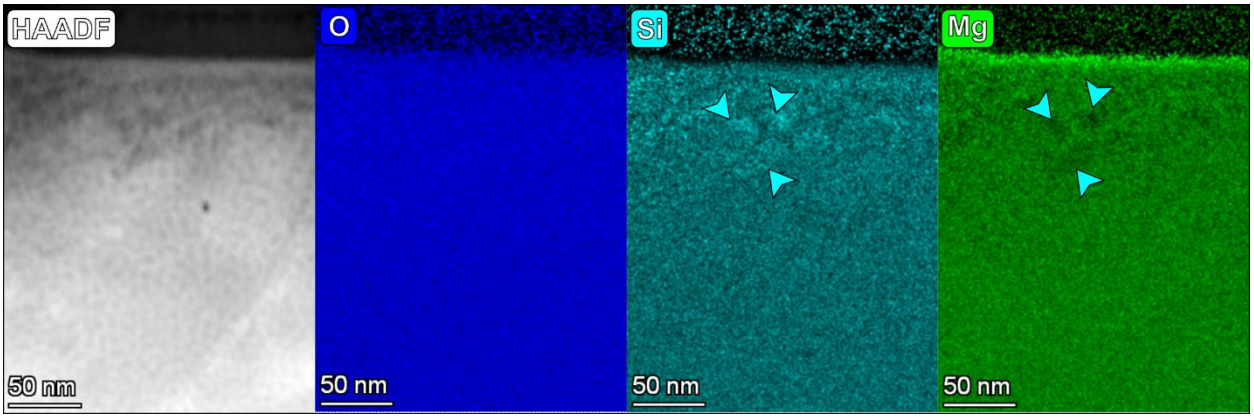

Figure S3. HAADF image (grayscale) and quantitative EDS elemental maps of the LF/LF H^+-irradiated olivine sample (O in blue, Si in cyan, and Mg in green). The elemental maps show the segregation of Si and Mg into rounded pockets within the ion-damaged region. A Mg-rich, Si-poor surface layer that is ~10 nm thick is also visible.

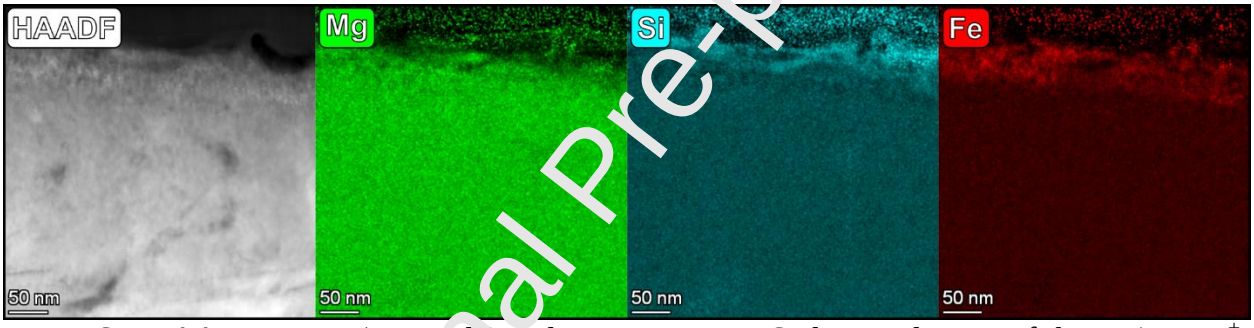

Figure S4. HAADF image (grayscale) and quantitative EDS elemental maps of the LF/LF He^+-irradiated olivine sample (Mg in green, Si in cyan, and Fe in red). The elemental maps show a region where Si and Mg segregation occurs in layers and Fe-enrichment extends to ~55 nm below the surface.

References

Abe, M., Takagi, Y., Kitazato, K., Abe, S., Hiroi, T., Vilas, F., Clark, B.E., Abell, P.A., Lederer, S.M., Jarvis, K.S., Nimura, T., Ueda, Y., Fujiwara, A., 2006. Near-infrared spectral results of asteroid Itokawa from the Hayabusa spacecraft. Science (80-.). 312, 1334–1338. https://doi.org/10.1126/science.1125718

Barber, D.J., 1981. Matrix phyllosilicates and associated minerals in C2M carbonaceous chondrites. Geochim. Cosmochim. Acta 45, 945–970.

Barr, T.L., Seal, S., 1995. Nature of the use of adventitious carbon as a binding energy standard. J. Vac. Sci. Technol. A 13, 1239–1246.

Beck, P., Quirico, E., Montes-Hernandez, G., Bonal, L., Bollard, J., Orthous-Daunay, F.-R., Howard, K., Schmitt, B., Brissaud, O., 2010. Hydrous mineralogy of CM and CI chondrites from infrared spectroscopy and their relationship wiht low albedo asteroids, in: 41st Lunar and Planetary Science Conference. p. 1586.

Berger, E.L., Keller, L.P., 2015. Solar flare track exposure ages in regolith particles: A calibration for transmission electron microscope measurements, in: 46th Lunar and Planetary Science Conference. p. 1543.

Biesinger, M.C., Payne, B.P., Grosvenor, A.P., Lau, L.W.M., Gerson, A.R., Smart, R.S.C., 2011. Resolving surface chemical states in XPS analysis of first row transition metals, oxides and hydroxides: Cr, Mn, Fe, Co and Ni. Appl. Surf. Sci. 257, 2717–2730. https://doi.org/10.1016/j.apsusc.2010.10.051

Bishop, J.L., Michalski, J.R., Carter, J., 2017. Remote Detection of Clay Minerals, 1st ed, Developments in Clay Science. Elsevier Ltd. https://doi.org/10.1016/B978-0-08-100355-8.00014-X

Bland, P.A., Cressey, G., Menzies, O.N., 2004. Modal mineralogy of carbonaceous chondrites by X-ray diffraction and Mössbauer spectroscopy. Meteorit. Planet. Sci. 39, 3–16. https://doi.org/10.1111/j.1945-5100.2004.tb00046.x

Bradley, J.P., Dukes, C., Baragiola, R., McFadden, L., Johnson, R.E., Brownlee, D.E., 1996. Radiation processing and the origins of interplanetary dust, in: 27th Lunar and Planetary Science Conference. pp. 149–150.

Brownlee, D.E., Joswiak, D.J., Bradley, J.P., Schlutter, D.J., Pepin, R.O., 1998. Tiny bubbles: Direct observation of He in IDPs, in: 29th Lunar and Planetary Science Conference. p. 1869.

Brunetto, R., Lantz, C., Ledu, D., Baklouti, D., Barucci, M.A., Beck, P., Delauche, L., Dionnet, Z., Dumas, P., Duprat, J., Engrand, C., Jamme, F., Oudayer, P., Quirico, E., Sandt, C., Dartois, E., 2014. Ion irradiation of Allende meteorite probed by visible, IR, and Raman spectroscopies. Icarus 237, 278–292. https://doi.org/10.1016/j.icarus.2014.04.047

Brunetto, R., Strazzulla, G., 2005. Elastic collisions in ion irradiation experiments: A mechanism for space weathering of silicates. Icarus 179, 265–273. https://doi.org/10.1016/j.icarus.2005.07.001

Buening, D.K., Buseck, P.R., 1973. Fe-Mg lattice diffusion in olivine. J. Geophys. Res. 78, 6852–6862.

Burgess, K.D., Stroud, R.M., 2021. Comparison of space weathering features in three particles from Itokawa. Meteorit. Planet. Sci. 56, 1109–1124. https://doi.org/10.1111/maps.13692

Carrez, P., Demyk, K., Cordier, P., Gengembre, L., Grimblot, J., D'Hendecourt, L., Jones, A.P., Leroux, H., 2002. Low-energy helium ion irradiation-induced amorphization and chemical

changes in olivine: Insights for silicate dust evolution in the interstellar medium. Meteorit. Planet. Sci. 37, 1599–1614. https://doi.org/10.1111/j.1945-5100.2002.tb00814.x

Carrez, P., Leroux, H., Cordier, P., Guyot, F., 2001. Electron-irradiation-induced phase transformation and fractional volatilization in (Mg, Fe)2SiO4olivine thin films. Philos. Mag. A Phys. Condens. Matter, Struct. Defects Mech. Prop. 81, 2823–2840. https://doi.org/10.1080/01418610108217167

Chakraborty, S., Farver, J.R., Yund, R.A., Rubie, D.C., 1994. Mg tracer diffusion in synthetic forsterite and San Carlos olivine as a function of P, T and fO2. Phys Chem Miner. 21, 489–500.

Chamberlin, S., Christoffersen, R., Keller, L., 2008. Space plasma ion processing of the lunar soil: Modeling of radiation-damaged rim widths on lunar grains, in: 36th Lunar and Planetary Science Conference. p. 2302.

Chaves, L.C., Thompson, M.S., 2022. Space weathering signatures in sulfide and silicate minerals from asteroid Itokawa. Earth, Planets Sp. 74. https://doi.org/10.1186/s40623-022-01683-6

Chaves, L.C., Thompson, M.S., Loeffler, M.J., Dukes, C.A., Szabo, P.S., Horgan, B.H.N., 2023. Evaluating the effects of space weathering on magnetite on airless planetary bodies. Icarus 402, 115634. https://doi.org/10.1016/j.icarus.2023.115634

Cheng, Y.-T., Simko, S.J., Militello, M.C., Dow, K.A., Auner, G.W., Alkaisi, M.H., Padmanabhan, K.R., 1992. A comparison between high- and low-energy ion mixing at different temperatures. Nucl. Instruments Methods Phys. Res. B 64, 38–47.

Christoffersen, R., Keller, L.P., 2015. Solar ion processing of Itokawa grains: Constraints on surface exposure times, in: 46th Lunar and Planetary Science Conference. p. 2084.

Christoffersen, R., Keller, L.P., Dukes, C., 2020. The role of solar wind ion processing in space weathering of olivine: Unraveling the paradox of laboratory irradiation results compared to observations of natural samples, in: 51st Lunar and Planetary Science Conference. p. 2147.

Christoffersen, R., Keller, L.P., Dukes, C., Rahman, Z., Baragiola, R., 2010. Experimental investigation of space radiation processing in lunar soil Ilmenite: Combining perspectives from surface science and transmission electron microscopy, in: 41st Lunar and Planetary Science Conference. p. 1532.

Christoffersen, R., Keller, L.P., Mckay, D.S., 1996. Microstructure, chemistry, and origin of grain rims on ilmenite from the lunar soil finest fraction. Meteorit. Planet. Sci. 31, 835–848. https://doi.org/10.1111/j.1945-5100.1996.tb02117.x

Clark, B.E., Binzel, R.P., Howell, E.S., Cloutis, E.A., Ockert-Bell, M., Christensen, P., Barucci, M.A., DeMeo, F., Lauretta, D.S., Connolly, H., Soderberg, A., Hergenrother, C., Lim, L., Emery, J., Mueller, M., 2011. Asteroid (101955) 1999 RQ36: Spectroscopy from 0.4 to 2.4 μm and meteorite analogs. Icarus 216, 462–475. https://doi.org/10.1016/j.icarus.2011.08.021

Clark, B.E., Sen, A., Zou, X.D., DellaGiustina, D.N., Sugita, S., Sakatani, N., Thompson, M., Trang, D., Tatsumi, E., Barucci, M.A., Barker, M., Campins, H., Morota, T., Lantz, C., Hendrix, A.R., Vilas, F., Keller, L., Hamilton, V.E., Kitazato, K., Sasaki, S., Matsuoka, M., Nakamura, T., Praet, A., Ferrone, S.M., Hiroi, T., Kaplan, H.H., Bottke, W.F., Li, J.Y., Le Corre, L., Molaro, J.L., Ballouz, R.L., Hergenrother, C.W., Rizk, B., Burke, K.N., Bennett, C.A., Golish, D.R., Howell, E.S., Becker, K., Ryan, A.J., Emery, J.P., Fornasier, S., Simon, A.A., Reuter, D.C., Lim, L.F., Poggiali, G., Michel, P., Delbo, M., Barnouin, O.S., Jawin, E.R., Pajola, M., Riu, L., Okada, T., Deshapriya, J.D.P., Brucato, J.R., Binzel, R.P.,

Lauretta, D.S., 2023. Overview of the search for signs of space weathering on the low-albedo asteroid (101955) Bennu. Icarus 400, 115563. https://doi.org/10.1016/j.icarus.2023.115563

Claverie, A., Roumili, A., Gessinn, N., Beauvillain, J., 1991. On the amorphization of silicon by light ion implantation: Ion flux and substrate temperature effects, in: Materials Research Society Symposium Proceedings. pp. 369–374.

Cloutis, E.A., Hiroi, T., Gaffey, M.J., Alexander, C.M.O., Mann, P., 2011a. Spectral reflectance properties of carbonaceous chondrites: 1. CI chondrites. Icarus 212, 180–209. https://doi.org/10.1016/j.icarus.2010.12.009

Cloutis, E.A., Hudon, P., Hiroi, T., Gaffey, M.J., 2012. Spectral reflectance properties of carbonaceous chondrites 4: Aqueously altered and thermally metamorphosed meteorites. Icarus 220, 586–617. https://doi.org/10.1016/j.icarus.2012.05.018

Cloutis, E.A., Hudon, P., Hiroi, T., Gaffey, M.J., Mann, P., 2011b. Spectral reflectance properties of carbonaceous chondrites: 2. CM chondrites. Icarus 216, 309–346. https://doi.org/10.1016/j.icarus.2011.09.009

Court, R.W., Sephton, M.A., 2012. Insights into the nature of cometary organic matter from terrestrial analogues. Int. J. Astrobiol. 11, 83–92. https://doi.org/10.1017/S1473550411000383

Court, R.W., Sephton, M.A., Parnell, J., Gilmour, I., 2006. The alteration of organic matter in response to ionising irradiation: Chemical trends and implications for extraterrestrial sample analysis. Geochim. Cosmochim. Acta 70, 1020–1039. https://doi.org/10.1016/j.gca.2005.10.017

Cymes, B.A., Burgess, K.D., Stroud, R.M., 2022. Helium-bearing "vesicular" nanophase metallic iron particles in lunar regolith grains, in: Lunar and Planetary Science Conference LIII. p. 2036.

Cymes, B.A., Burgess, K.D., Stroud, R.M., Team, and the A.S., 2023. Comparison of space weathered lunar olivines of varying maturity, recent exposure, and curation temperature, in: Lunar and Planetary Science Conference LIV. p. 2599.

DellaGiustina, D.N., Burke, K.N., Walsh, K.J., Smith, P.H., Golish, D.R., Bierhaus, E.B., Ballouz, L., Becker, T.L., Campins, H., Tatsumi, E., Yumoto, K., Sugita, S., Prasanna Deshapriya, J.D., Cloutis, E.A., Clark, B.E., Hendrix, A.R., Sen, A., Al Asad, M.M., Daly, M.G., Applin, D.M., Avdellidou, C., Barucci, M.A., Becker, K.J., Bennett, C.A., Bottke, W.F., Brodbeck, J.F., Connolly Jr., H.C., Delbo, M., de Leon, J., Drouet d'Aubigny, C.Y., Edmundson, K.L., Fornasier, S., Hamilton, V.E., Hasselmann, P.H., Hergenrother, C.W., Howell, E.S., Jawin, E.R., Kaplan, H.H., Le Corre, L., Lim, L.F., Li, J.Y., Michel, P., Molaro, J.L., Nolan, M.C., Nolau, J., Pajola, M., Parkinson, A., Popescu, M., Porter, N.A., Rizk, B., Rizos, J.L., Ryan, A.J., Rozitis, B., Shultz, N.K., Simon, A.A., Trang, D., Van Auken, R.B., Wolner, C.W. V., Lauretta, D.S., 2020. Variations in color and reflectance on the surface of asteroid (101955) Bennu. Science (80-.). 370, eabc3660. https://doi.org/10.1126/science.abc3660

Demyk, K., Carrez, P., Leroux, H., Cordier, P., Jones, A.P., Borg, J., Quirico, E., Raynal, P.I., D'Hendecourt, L., 2001. Structural and chemical alteration of crystalline olivine under low energy He+ irradiation. Astron. Astrophys. 368, L38–L41. https://doi.org/10.1051/0004-6361:20010208

Dohmen, R., Chakraborty, S., Becker, H.W., 2002. Si and O diffusion in olivine and implications for characterizing plastic flow in the mantle. Geophys. Res. Lett. 29, 26-1-26–4.

https://doi.org/10.1029/2002GL015480

Dukes, C.A., Baragiola, R.A., McFadden, L.A., 1999. Surface modification of olivine by H+ and He+ bombardment. J. Geophys. Res. Planets 104, 1865–1872. https://doi.org/10.1029/98JE02820

Dukes, C.A., Fulvio, D., Baragiola, R.A., 2015. Ion-irradiation induced changes in the surface composition of carbonaceous meteorites, in: Space Weathering of Airless Bodies: An Integration of Remote Sensing Data, Laboratory Experiments and Sample Analysis Workshop. p. 2063.

Gailliard, J.P., 1984. Recoil implantation and ion mixing, in: Kossowsky, R., Singhal, S.C. (Eds.), Surface Engineering: Surface Modification of Materials. Springer Dordrecht, pp. 32–47. https://doi.org/10.1007/978-94-009-6216-3_2

Gillis-Davis, J.J., Gasda, P.J., Bradley, J.P., Ishii, H.A., Bussey, D.B.J., 2015. Laser space weathering of Allende (CV2) and Murchison (CM2) carbonaceous chondrites, in: 46th Lunar and Planetary Science Conference. p. 1607. https://doi.org/10.1029/2012JE004137.

Gillis-Davis, J.J., Lucey, P.G., Bradley, J.P., Ishii, H.A., Connolly, H.C., 2013. Laser space weathering of Allende meteorite, in: 44th Lunar and Planetary Science Conference. p. 2494.

Gillis-Davis, J.J., Lucey, P.G., Bradley, J.P., Ishii, H.A., Kaluna, H.M., Misra, A., Connolly, H.C., 2017. Incremental laser space weathering of Allende reveals non-lunar like space weathering effects. Icarus 286, 1–14. https://doi.org/10.1016/j.icarus.2016.12.031

Glavin, D.P., Conel, M.O., Aponte, J.C., Dworkin, J.P., Elsila, J.E., Yabuta, H., 2018. The origin and evolution of organic matter in carbonaceous chondrites and links to their parent bodies, in: Primitive Meteorites and Asteroids: Physical, Chemical, and Spectroscopic Observations Paving the Way to Exploration. Elsevier, pp. 205–271. https://doi.org/10.1016/B978-0-12-813325-5.00003-3

Glotch, T.D., Bandfield, J.L., Lucey, P.G., Hayne, P.O., Greenhagen, B.T., Arnold, J.A., Ghent, R.R., Paige, D.A., 2015. Formation of lunar swirls by magnetic field standoff of the solar wind. Nat. Commun. 6, 6189. https://doi.org/10.1038/ncomms7189

Hamilton, V.E., Simon, A.A., Christensen, P.R., Reuter, D.C., Clark, B.E., Barucci, M.A., Bowles, N.E., Boynton, W.V., Brucato, J.R., Cloutis, E.A., Connolly, H.C., Donaldson Hanna, K.L., Emery, J.P., Enos, H.L., Fornasier, S., Haberle, C.W., Hanna, R.D., Howell, E.S., Kaplan, H.H., Keller, L.P., Lantz, C., Li, J.Y., Lim, L.F., McCoy, T.J., Merlin, F., Nolan, M.C., Praet, A., Rozitis, B., Sandford, S.A., Schrader, D.L., Thomas, C.A., Zou, X.D., Lauretta, D.S., 2019. Evidence for widespread hydrated minerals on asteroid (101955) Bennu. Nat. Astron. 3, 332–340. https://doi.org/10.1038/s41550-019-0722-2

Hapke, B., 2001. Space weathering from Mercury to the asteroid belt. J. Geophys. Res. 106, 10039–10073. https://doi.org/https://doi.org/10.1029/2000JE001338

Hapke, B., 1973. Darkening of silicate rock powders by solar wind sputtering. Moon 7, 342–355. https://doi.org/10.1007/BF00564639

Harries, D., Langenhorst, F., 2014. The mineralogy and space weathering of a regolith grain from 25143 Itokawa and the possibility of annealed solar wind damage. Earth, Planets Sp. 66, 1–11. https://doi.org/10.1186/s40623-014-0163-1

Haynes, T.E., Holland, O.W., 1991. Comparative study of implantation-induced damage in GaAs and Ge: Temperature and flux dependence. Appl. Phys. Lett. 59, 452–454. https://doi.org/10.1063/1.105460

Hendrix, A.R., Vilas, F., Li, J.Y., 2016. The UV signature of carbon in the solar system. Meteorit. Planet. Sci. 51, 105–115. https://doi.org/10.1111/maps.12575

Hermeling, J., Schmalzried, H., 1984. Tracerdiffusion of the Fe-cations in olivine (FexMg1-x)2SiO4 (III). Phys. Chem. Miner. 11, 161–166. https://doi.org/10.1007/BF00387846

Hiroi, T., Abe, M., Kitazato, K., Abe, S., Clark, B.E., Sasaki, S., Ishiguro, M., Barnouin-Jha, O.S., 2006. Developing space weathering on the asteroid 25143 Itokawa. Nature 443, 56–58. https://doi.org/10.1038/nature05073

Hiroi, T., Sasaki, S., Misu, T., Nakamura, T., 2013. Keys to detect space weathering on Vesta: Changes of visible and near-infrared reflectance spectra of HEDs and carbonaceous chondrites, in: 44th Lunar and Planetary Science Conference. Lunar and Planetary Institute, The Woodlands, p. 1276.

Ho, P.S., 1978. Effects of enhanced diffusion on preferred sputtering of homogeneous alloy surfaces. Surf. Sci. 72, 253–263. https://doi.org/10.1016/0039-6028(78)90294-7

Hood, L.L., Schubert, G., 1980. Lunar magnetic anomalies and surface optical properties. Science (80-.). 208, 49–51.

Johnson, R.E., 1990. Energetic Charged-Particle Interactions with Atmospheres and Surfaces. Springer-Verlag Berlin Heidelberg. https://doi.org/10.1007/978-3-642-48375-2

Johnson, R.E., 1989. Application of laboratory data to the sputtering of a planetary regolith. Icarus 78, 206–210.

Johnson, T. V., Fanale, F.P., 1973. Optical properties of carbonaceous chondrites and their relationship to asteroids. J. Geophys. Res. 78, 8507–8518. https://doi.org/10.1029/jb078i035p08507

Jones, A.P., 2012. Variations on a theme-the evolution of hydrocarbon solids: II. Optical property modelling-the optEC(s) model. Astron. Astrophys. 540, 1–21. https://doi.org/10.1051/0004-6361/201117624

Kaluna, H.M., Ishii, H.A., Bradley, J.P., Gillis-Davis, J.J., Lucey, P.G., 2017. Simulated space weathering of Fe- and Mg-rich aqueously altered minerals using pulsed laser irradiation. Icarus 292, 245–258. https://doi.org/10.1016/j.icarus.2016.12.028

Kaplan, H.H., Simon, A.A., Hamilton, V.E., Thompson, M.S., Sandford, S.A., Barucci, M.A., Cloutis, E.A., Brucato, J., Reuter, D.C., Glavin, D.P., Clark, B.E., Dworkin, J.P., Campins, H., Emery, J.P., Fornasier, S., Zou, X.D., Lauretta, D.S., 2021. Composition of organics on asteroid (101955) Bennu. Astron. Astrophys. 653, 1–11. https://doi.org/10.1051/0004-6361/202141167

Keller, L.P., Berger, E.L., 2014. A transmission electron microscope study of Itokawa regolith grains. Earth, Planets Sp. 66, 71. https://doi.org/10.1186/1880-5981-66-71

Keller, L.P., Berger, E.L., Christoffersen, R., Zhang, S., 2016. Direct determination of the space weathering rates in lunar soils and Itokawa regolith from sample analyses, in: 47th Lunar and Planetary Science Conference. p. 2525.

Keller, L.P., Berger, E.L., Zhang, S., Christoffersen, R., Sandford, S., 2021. Solar energetic particle tracks in lunar samples: A transmission electron microscope calibration and implications for lunar space weathering. Meteorit. Planet. Sci. 1707, 1685–1707. https://doi.org/10.1111/maps.13732

Keller, L.P., Christoffersen, R., Dukes, C.A., Baragiola, R.A., Rahman, Z., 2015a. Fe and O EELS studies of ion irradiated Murchison CM2 carbonaceous chondrite matrix, in: 78th Annual Meeting of the Meteoritical Society. p. 5354.

Keller, L.P., Christoffersen, R., Dukes, C.A., Baragiola, R.A., Rahman, Z., 2015b. Ion irradiation experiments on the Murchison CM2 carbonaceous chondrite: Simulating space weathering of primitive asteroids, in: 46th Lunar and Planetary Science Conference. p. 1913.

Keller, L.P., Christoffersen, R., Dukes, C.A., Baragiola, R.A., Rahman, Z., 2015c. Experimental space weathering of carbonaceous chondrite matrix, in: Space Weathering of Airless Bodies: An Integration of Remote Sensing Data, Laboratory Experiments and Sample Analysis Workshop. p. 2010.

Keller, L.P., McKay, D.S., 1997. The nature and origin of rims on lunar soil grains. Geochim. Cosmochim. Acta 61, 2331–2341. https://doi.org/10.1016/S0016-7037(97)00085-9

Keller, L.P., McKay, D.S., 1993. Discovery of vapor deposits in the lunar regolith. Science (80-.). 261, 1305–1307. https://doi.org/10.1126/science.261.5126.1305

Keller, L.P., Zhang, S., 2015. Rates of space weatheirng in lunar soils, in: Space Weathering of Airless Bodies: An Integration of Remote Sensing Data, Laboratory Experiments and Sample Analysis Workshop. p. 2056.

Kelly, R., Sanders, J.B., 1976. On the role of recoil implantation in altering the stoichiometry of a bombarded solid. Nucl. Instruments Methods 132, 335–343. https://doi.org/10.1016/0029-554X(76)90755-2

Kling, A.M., Greer, J., Thompson, M.S., Heck, P.R., Isheim, D., Seidman, D., 2023. Solar wind-sourced water stored in nanoscale reservoirs in lunar soil grains, in: Lunar and Planetary Science Conference LIV. p. 1710.

Kramer, G.Y., Besse, S., Dhingra, D., Nettles, J., Klima, R., Garrick-Bethell, I., Clark, R.N., Combe, J.P., Head, J.W., Taylor, L.A., Pieters, C.M., Boardman, J., McCord, T.B., 2011. M3 spectral analysis of lunar swirls and the link between optical maturation and surface hydroxyl formation at magnetic anomalies. J. Geophys. Res. 116, E00G18. https://doi.org/https://doi.org/10.1029/2010JE003729

Laczniak, D.L., Thompson, M.S., 2023. Space weathering effects revealed through in situ ion irradiation and heating of the Murchison meteorite in the transmission electron microscope, in: Lunar and Planetary Science Conference LIV. p. 1176.

Laczniak, D.L., Thompson, M.S., Christoffersen, R., Dukes, C.A., Clemett, S.J., Morris, R. V., Keller, L.P., 2021. Characterizing the spectral, microstructural, and chemical effects of solar wind irradiation on the Murchison carbonaceous chondrite through coordinated analyses. Icarus 364, 114479. https://doi.org/10.1016/j.icarus.2021.114479

Lantz, C., Brunetto, R., Barucci, M.A., Dartois, E., Duprat, J., Engrand, C., Godard, M., Ledu, D., Quirico, E., 2015. Ion irradiation of the Murchison meteorite: Visible to mid-infrared spectroscopic results. Astron. Astrophys. 577, A41. https://doi.org/10.1051/0004-6361/201425398

Lantz, C., Brunetto, R., Barucci, M.A., Fornasier, S., Baklouti, D., Bourçois, J., Godard, M., 2017. Ion irradiation of carbonaceous chondrites: A new view of space weathering on primitive asteroids. Icarus 285, 43–57. https://doi.org/10.1016/j.icarus.2016.12.019

Lauretta, D.S., Enos, H.L., Polit, A.T., Roper, H.L., Wolner, C.W. V, 2021. OSIRIS-REx at Bennu: Overcoming challenges to collect a sample of the early Solar System, in: Longobardo, A. (Ed.), Sample Return Missions. Elsevier Inc., pp. 163–194. https://doi.org/10.1016/c2018-0-03374-5

Li, Y., Li, X., Wang, S., Li, S., Tang, H., Coulson, I.M., 2013. Crystal orientation results in different amorphization of olivine during solar wind implantation. J. Geophys. Res. E Planets 118, 1974–1982. https://doi.org/10.1002/jgre.20151

Loeffler, M.J., Baragiola, R.A., Murayama, M., 2008. Laboratory simulations of redeposition of impact ejecta on mineral surfaces. Icarus 196, 285–292. https://doi.org/10.1016/j.icarus.2008.02.021

Loeffler, M.J., Dukes, C.A., Baragiola, R.A., 2009. Irradiation of olivine by 4 keV He+: Simulation of space weathering by the solar wind. J. Geophys. Res. 114, E03003. https://doi.org/10.1029/2008JE003249

Matsumoto, T., Noguchi, T., Miyake, A., Igami, Y., Haruta, M., Saito, H., Hata, S., Seto, Y., Tomioka, N., Yurimoto, H., Nakamura, T., Yabuta, H., Naraoka, H., Okazaki, R., Sakamoto, K., Tachibana, S., Watanabe, S., Tsuda, Y., Sub-team, H.M.-P.F., 2022. Space weathering of anhydrous minerals in regolith samples from the C-type asteroid ryug, in: Lunar and Planetary Science Conference LIII. p. 1693.

Matsumoto, Toru, Tsuchiyama, A., Miyake, A., Noguchi, T., Nakamura, M., Uesugi, K., Takeuchi, A., Suzuki, Y., Nakano, T., 2015. Surface and internal structures of a space-weathered rim of an Itokawa regolith particle. Icarus 257, 230–238. https://doi.org/10.1016/j.icarus.2015.05.001

Matsumoto, T., Tsuchiyama, A., Miyake, A., Noguchi, T., Nakamura, T., Nakamura, M., Matsuno, J., Shimada, A., Uesugi, K., Nakano, T., 2014. Surface micromorphologies of regolith particles from asteroid Itokawa and its implication to space weathering, in: 77th Annual Meteoritical Society Meeting. p. 5130.

Matsumoto, T., Tsuchiyama, A., Watanabe, N., Yasuda, Y., Miyake, A., Nakauchi, Y., Okada, T., Abe, M., Yada, T., Uesugi, M., Karouji, Y., Nakano, A., Hashiguchi, M., Kumagai, K., 2015. Systematic ion irradiation experiments to olivine: Comparison with space weathered rims of Itokawa regolith particles, in: Space Weathering of Airless Bodies. p. 2045.

Matsuoka, M., Nakamura, T., Hiroi, T., Okumura, S., Sasaki, S., 2020. Space weathering simulation with low-energy laser irradiation of Murchison CM chondrite for reproducing micrometeoroid bombardments on C-type asteroids. Astrophys. J. 890, L23. https://doi.org/10.3847/2041-8213/ab72a4

Matsuoka, M., Nakamura, T., Kimura, Y., Hiroi, T., Nakamura, R., Okumura, S., Sasaki, S., 2015. Pulse-laser irradiation experiments of Murchison CM2 chondrite for reproducing space weathering on C-type asteroids. Icarus 254, 135–143. https://doi.org/10.1016/j.icarus.2015.02.029

Melendez, L.E., Thompson, M.S., Keller, L.P., Snead, C.J., 2023. Characterizing space weathering features in grains from asteroid Ryugu, in: 54th Lunar and Planetary Science Conference. p. 2069. https://doi.org/10.1038/s41550-022-01841-6

Milliken, R.E., Mustard, J.F., 2007. Estimating the water content of hydrated minerals using reflectance spectroscopy. I. Effects of darkening agents and low-albedo materials. Icarus 189, 550–573. https://doi.org/10.1016/j.icarus.2007.02.017

Moroz, L., Baratta, G., Strazzulla, G., Starukhina, L., Dotto, E., Barucci, M.A., Arnold, G., Distefano, E., 2004. Optical alteration of complex organics induced by ion irradiation: 1. Laboratory experiments suggest unusual space weathering trend. Icarus 170, 214–228. https://doi.org/10.1016/j.icarus.2004.02.003

Nakamura, T., Noguchi, T., Tanaka, M., Zolensky, M.E., Kimura, M., Tsuchiyama, A., Nakato, A., Ogami, T., Ishida, H., Uesugi, M., Yada, T., Shirai, K., Fujimura, A., Okazaki, R., Sandford, S.A., Ishibashi, Y., Abe, M., Okada, T., Ueno, M., Mukai, T., Yoshikawa, M., Kawaguchi, J., 2011. Itokawa dust particles: A direct link between S-type asteroids and ordinary chondrites. Science (80-.). 333, 1113–1116. https://doi.org/10.1126/science.1207758

Nakato, A., Yada, T., Nishimura, M., Yogata, K., Miyazaki, A., Nagashima, K., Hatakeda, K., Kumagai, K., Hitomi, Y., Soejima, H., Bibring, J.P., Pilorget, C., Hamm, V., Brunetto, R.,

Riu, L., Lourit, L., Loizeau, D., Le Pivert-Jolivet, T., Lequertier, G., Moussi-Soffys, A., Abe, M., Okada, T., Usui, T., Nakazawa, S., Saiki, T., Tanaka, S., Terui, F., Yoshikawa, M., Watanabe, S., Tsuda, Y., 2023. Variations of the surface characteristics of Ryugu returned samples. Earth, Planets Sp. 75, 45. https://doi.org/10.1186/s40623-022-01754-8

Nastar, M., Soisson, F., 2012. Radiation-Induced Segregation, in: Konings, R.J.M. (Ed.), Comprehensive Nuclear Materials. Elsevier, Amsterdam, pp. 471–496. https://doi.org/10.1016/B978-0-08-056033-5.00035-5

Noble, S.K., Keller, L.P., Pieters, C.M., 2005. Evidence of space weathering in regolith breccias I: Lunar regolith breccias. Meteorit. Planet. Sci. 40, 397–408. https://doi.org/https://doi.org/10.1111/j.1945-5100.2010.01151.x

Noguchi, T., Bridges, J.C., Hicks, L.J., Gurman, S.J., Kimura, M., Hashimoto, T., Konno, M., Bradley, J.P., Okazaki, R., Uesugi, M., Yada, T., Karouji, Y., Abe, M., Okada, T., Mitsunari, T., Nakamura, T., Kagi, H., 2014a. Mineralogy of four Itokawa particles collected from the first touchdown site. Earth, Planets Sp. 66, 124. https://doi.org/10.1186/1880-5981-66-124

Noguchi, T., Kimura, M., Hashimoto, T., Konno, M., Nakamura, T., Zolensky, M.E., Okazaki, R., Tanaka, M., Tsuchiyama, A., Nakato, A., Ogami, T., Ishida, H., Sagae, R., Tsujimoto, S., Matsumoto, T., Matsuno, J., Fujimura, A., Abe, M., Yada, T., Mukai, T., Ueno, M., Okada, T., Shirai, K., Ishibashi, Y., 2014b. Space weathered rims found on the surfaces of the Itokawa dust particles. Meteorit. Planet. Sci. 49, 188–214. https://doi.org/10.1111/maps.12111

Noguchi, T., Matsumoto, T., Miyake, A., Igami, Y., Haruta, M., Saito, H., Hata, S., Seto, Y., Miyahara, M., Tomioka, N., Ishii, H.A., Bradley, J.P., Ohtaki, K.K., Dobrică, E., Leroux, H., Le Guillou, C., Jacob, D., de la Peña, F., Laforet, S., Marinova, M., Langenhorst, F., Harries, D., Beck, P., Phan, T.H.V., Rebois, R., Abreu, N.M., Gray, J., Zega, T., Zanetta, P.M., Thompson, M.S., Stroud, R., Burgess, K., Cymes, B.A., Bridges, J.C., Hicks, L., Lee, M.R., Daly, L., Bland, P.A., Zolensky, M.E., Frank, D.R., Martinez, J., Tsuchiyama, A., Yasutake, M., Matsuno, J., Okumura, S., Mitsukawa, I., Uesugi, K., Uesugi, M., Takeuchi, A., Sun, M., Enju, S., Tokigawa, A., Michikami, T., Nakamura, T., Matsumoto, M., Nakauchi, Y., Abe, M., Arakawa, M., Fujii, A., Hayakawa, M., Hirata, Naru, Hirata, Naoyuki, Honda, R., Honda, C., Hosoda, S., Iijima, Y. ichi, Ikeda, H., Ishiguro, M., Ishihara, Y., Iwata, T., Kawahara, K., Kikuchi, S., Kitazato, K., Matsumoto, K., Matsuoka, M., Mimasu, Y., Miura, A., Morota, T., Nakazawa, S., Namiki, N., Noda, H., Noguchi, R., Ogawa, N., Ogawa, K., Okada, T., Okamoto, C., Ono, G., Ozaki, M., Saiki, T., Sakatani, N., Sawada, H., Senshu, H., Shimaki, Y., Shirai, K., Sugita, S., Takei, Y., Takeuchi, H., Tanaka, S., Tatsumi, E., Terui, F., Tsukizaki, R., Wada, K., Yamada, M., Yamada, T., Yamamoto, Y., Yano, H., Yokota, Y., Yoshihara, K., Yoshikawa, M., Yoshikawa, K., Fukai, R., Furuya, S., Hatakeda, K., Hayashi, T., Hitomi, Y., Kumagai, K., Miyazaki, A., Nakato, A., Nishimura, M., Soejima, H., Suzuki, A.I., Usui, T., Yada, T., Yamamoto, D., Yogata, K., Yoshitake, M., Connolly, H.C., Lauretta, D.S., Yurimoto, H., Nagashima, K., Kawasaki, N., Sakamoto, N., Okazaki, R., Yabuta, H., Naraoka, H., Sakamoto, K., Tachibana, S., Watanabe, S. ichiro, Tsuda, Y., 2022. A dehydrated space-weathered skin cloaking the hydrated interior of Ryugu. Nat. Astron. 7, 170–181. https://doi.org/10.1038/s41550-022-01841-6

Noguchi, T., Nakamura, T., Kimura, M., Zolensky, M.E., Tanaka, M., Hashimoto, T., Konno, M., Nakato, A., Ogami, T., Fujimura, A., Abe, M., Yada, T., Mukai, T., Ueno, M., Okada,

T., Shirai, K., Ishibashi, Y., Okazaki, R., 2011. Incipient space weathering observed on the surface of Itokawa dust particles. Science (80-.). 333, 1121–1125. https://doi.org/10.1126/science.1207794

Pieters, C.M., Noble, S.K., 2016. Space weathering on airless bodies. J. Geophys. Res. Planets 121, 1865–1884. https://doi.org/10.1038/175238c0

Pieters, C.M., Taylor, L.A., Noble, S.K., Keller, L.P., Hapke, B., Morris, R. V., Allen, C.C., McKay, D.S., Wentworth, S., 2000. Space weathering on airless bodies: Resolving a mystery with lunar samples. Meteorit. Planet. Sci. 35, 1101–1107. https://doi.org/https://doi.org/10.1111/j.1945-5100.2000.tb01496.x

Prince, B.S., Magnuson, M.P., Chaves, L.C., Thompson, M.S., Loeffler, M.J., 2020. Space Weathering of FeS Induced via Pulsed Laser Irradiation. J. Geophys. Res. Planets 125, e2019JE006242. https://doi.org/10.1029/2019JE006242

Rubino, S., Potin, S., Lantz, C., Baklouti, D., Beck, P., Brissaud, O., Leroux, H., Quirico, E., Schmitt, B., Borondics, F., Brunetto, R., 2022. Geometry induced bias in the remote near-IR identification of phyllosilicates on space weathered bodies. Icarus 376, 114887. https://doi.org/10.1016/j.icarus.2022.114887

Sasaki, S., Nakamura, K., Hamabe, Y., Kurahashi, E., Hiroi, T., 2001. Production of iron nanoparticles by laser irradiation in a simulation of lunar-like space weathering. Nature 410, 555–557.

Schrempel, F., Jäger, C., Fabian, D., Dorschner, J., Henning, T., Wesch, W., 2002. Study of the amorphization process of MgSiO3 by ion irradiation as a form of dust processing in astrophysical environments. Nucl. Instruments Methods Phys. Res. Sect. B Beam Interact. with Mater. Atoms 191, 411–415. https://doi.org/10.1016/S0168-583X(02)00553-0

Sephton, M.A., 2002. Organic compounds in carbonaceous meteorites. Nat. Prod. Rep. 19, 292–311. https://doi.org/10.1039/b103775g

Sigmund, P., 1981. Sputtering by Ion Bombardment: Theoretical Concepts, in: Behrisch, R. (Ed.), Sputtering by Particle Bombardment I. Springer-Verlag Berlin Heidelberg, pp. 9–71. https://doi.org/https://doi.org/10.1007/3540105212_7

Sigmund, P., 1979. Recoil implantation and ion-beam-induced composition changes in alloys and compounds. J. Appl. Phys. 50, 7261. https://doi.org/https://doi.org/10.1063/1.325807

Simon, A.A., Kaplan, H.H., Hamilton, V.E., Lauretta, D.S., Campins, H., Emery, J.P., Barucci, M.A., DellaGiustina, D.N., Reuter, D.C., Sandford, S.A., Golish, D.R., Lim, L.F., Ryan, A., Rozitis, B., Bennett, C.A., 2020. Widespread carbon-bearing materials on near-Earth asteroid (101955) Bennu. Science (80-.). 370, eabc3522.

Takigawa, A., Asada, Y., Nakauchi, Y., Matsumoto, T., Tsuchiyama, A., Abe, M., Watanabe, N., 2019. H+ ion irradiation experiments of enstatite: Space weathering by solar wind, in: 82nd Annual Meeting of The Meteoritical Society. Sapporo, p. 6331.

Takir, D., Emery, J.P., Mcsween, H.Y., Hibbitts, C.A., Clark, R.N., Pearson, N., Wang, A., 2013. Nature and degree of aqueous alteration in CM and CI carbonaceous chondrites. Meteorit. Planet. Sci. 48, 1618–1637. https://doi.org/10.1111/maps.12171

Tamhane, A.S., Agrawal, J.K., 1979. Diffusion of rare gases of solar wind origin from lunar fines as bubbles. Earth Planet. Sci. Lett. 42, 243–250.

Taylor, L.A., Pieters, C.M., Keller, L.P., Morris, V., McKay, D.S., 2001. Lunar Mare Soils: Space weathering and the major effects of surface-correlated nanophase Fe. J. Geophys. Res. 106, 27985–27999.

Terranova, U., Mitchell, C., Sankar, M., Morgan, D., de Leeuw, N.H., 2018. Initial oxygen

incorporation in the prismatic surfaces of troilite FeS. J. Phys. Chem. C 122, 12810–12818. https://doi.org/10.1021/acs.jpcc.8b02774

Thomas, J.E., Skinner, W.M., Smart, R.S.C., 2003. A comparison of the dissolution behavior of troilite with other iron(II) sulfides; implications of structure. Geochim. Cosmochim. Acta 67, 831–843. https://doi.org/10.1016/S0016-7037(02)01146-8

Thompson, M.S., Christoffersen, R., Zega, T.J., Keller, L.P., 2014. Microchemical and structural evidence for space weathering in soils from asteroid Itokawa. Earth, Planets Sp. 66, 89. https://doi.org/10.1186/1880-5981-66-89

Thompson, M.S., Haenecour, P., Howe, J.Y., Laczniak, D.L., Zega, T.J., Hu, J., Chen, W., Keller, L.P., Christoffersen, R., 2019a. Simulating space weathering in the transmission electron microscope via dynamic in situ heating and helium irradiation of olivine, in: 50th Lunar and Planetary Science Conference. p. 1425.

Thompson, M.S., Loeffler, M.J., Morris, R. V., Keller, L.P., Christoffersen, R., 2019b. Spectral and chemical effects of simulated space weathering of the Murchison CM2 carbonaceous chondrite. Icarus 319, 499–511. https://doi.org/10.1016/j.icarus.2018.09.022

Thompson, M.S., Morris, R. V., Clemett, S.J., Loeffler, M.J., Trang, D., Keller, L.P., Christoffersen, R., Agresti, D.G., 2020. The effect of progressive space weathering on the organic and inorganic components of a carbonaceous chondrite. Icarus 346, 113775. https://doi.org/10.1016/j.icarus.2020.113775

Thompson, M.S., Zanetta, P.-M., Zega, T.J., Noguchi, T., Yurimoto, H., Nakamura, T., Yabuta, H., Naraoka, N., Okazaki, K., Sakamoto, K., Tachibana, S., Watanabe, S., Tsuda, Y., Hayabusa2 Min-Pet Fine Sub-team, 2022. Evidence for micrometeoroid bombardment on the surface of asteroid Ryugu, in: Lunar and Planetary Science Conference LIII. p. 2134.

Thompson, M.S., Zega, T.J., Becerra, P., Keane, J.T., Byrne, S., 2016. The oxidation state of nanophase Fe particles in lunar soil: Implications for space weathering. Meteorit. Planet. Sci. 51, 1082–1095. https://doi.org/10.1111/maps.12646

Thompson, M.S., Zega, T.J., Howe, J.Y., 2017. In situ experimental formation and growth of Fe nanoparticles and vesicles in lunar soil. Meteorit. Planet. Sci. 52, 413–427. https://doi.org/10.1111/maps.12798

Tomeoka, K., Buseck, P.R., 1985. Indicators of aqueous alteration in CM carbonaceous chondrites: Microtextures of a layered mineral containing Fe, S, O and Ni. Geochim. Cosmochim. Acta 49, 2149–2163. https://doi.org/10.1016/0016-7037(85)90073-0

Trang, D., Thompson, M.S., Clark, B.E., Kaplan, H.H., Zou, X., Li, J., Ferrone, S.M., Hamilton, V.E., Simon, A.A., Reuter, D.C., Keller, L.P., Barucci, M.A., Campins, H., Lantz, C., DellaGiustina, D.N., Ballouz, R.-L., Jawin, E.R., Connolly, Jr., H.C., Walsh, K.J., Lauretta, D.S., 2021. The Role of Hydrated Minerals and Space Weathering Products in the Bluing of Carbonaceous Asteroids. Planet. Sci. J. 2, 68. https://doi.org/10.3847/PSJ/abe76f

Vander Wal, R.L., Bryg, V.M., Hays, M.D., 2011. XPS analysis of combustion aerosols for chemical composition, surface chemistry, and carbon chemical state. Anal. Chem. 83, 1924–1930. https://doi.org/10.1021/ac102365s

Vernazza, P., Fulvio, D., Brunetto, R., Emery, J.P., Dukes, C.A., Cipriani, F., Witasse, O., Schaible, M.J., Zanda, B., Strazzulla, G., Baragiola, R.A., 2013. Paucity of Tagish Lake-like parent bodies in the asteroid belt and among Jupiter Trojans. Icarus 225, 517–525. https://doi.org/10.1016/j.icarus.2013.04.019

Wang, L.M., Ewing, R.C., 1992. Ion-beam-induced amorphization of complex ceramic materials—minerals. MRS Bull. 17, 38–44. https://doi.org/10.1557/S0883769400041270

Wang, L.M., Miller, M.L., Ewing, R.C., 1993. HRTEM study of displacement cascade damage in krypton-ion-irradiated silicate-olivine. Ultramicroscopy 51, 339–347.

Wang, Z., Hiraga, T., Kohlstedt, D.L., 2004. Effect of H+ on Fe-Mg interdiffusion in olivine, (Fe,Mg)2SiO4. Appl. Phys. Lett. 85, 209–211. https://doi.org/10.1063/1.1769593

Wehner, G., 1959. Influence of the angle of incidence on sputtering yields. J. Appl. Phys. 30, 1762–1765. https://doi.org/10.1063/1.1735051

Wirth, B.D., 2007. How does radiation damage materials? Science (80-.). 318, 923–924. https://doi.org/10.1126/science.318.5858.1866

Yada, T., Abe, M., Okada, T., Nakato, A., Yogata, K., Miyazaki, A., Hatakeda, K., Kumagai, K., Nishimura, M., Hitomi, Y., Soejima, H., Yoshitake, M., Iwamae, A., Furuya, S., Uesugi, M., Karouji, Y., Usui, T., Hayashi, T., Yamamoto, D., Fukai, R., Sugita, S., Cho, Y., Yumoto, K., Yabe, Y., Bibring, J.-P., Pilorget, C., Hamm, V., Brunetto, R., Riu, L., Lourit, L., Loizeau, D., Lequertier, G., Moussi-Soffys, A., Tachibana, S., Sawada, H., Okazaki, R., Takano, Y., Sakamoto, K., Miura, Y.N., Yano, H., Ireland, T.R., Yamada, T., Fujimoto, M., Kitazato, K., Namiki, N., Arakawa, M., Hirata, Naru, Yurimoto, H., Nakamura, T., Noguchi, T., Yabuta, H., Naraoka, H., Ito, M., Nakamura, E., Uesugi, K., Kobayashi, K., Michikami, T., Kikuchi, H., Hirata, Naoyuki, Ishihara, Y., Matsumoto, K., Noda, H., Noguchi, R., Shimaki, Y., Shirai, K., Ogawa, K., Wada, K., Senshu, H., Yamamoto, Y., Morota, T., Honda, R., Honda, C., Yokota, Y., Matsuoka, M., Sakatani, N., Tatsumi, E., Miura, A., Yamada, M., Fujii, A., Hirose, C., Hosoda, S., Ikeda, H., Iwata, T., Kikuchi, S., Mimasu, Y., Mori, O., Ogawa, N., Ono, G., Shimada, T., Soldini, S., Takahashi, T., Takei, Y., Takeuchi, H., Tsukizaki, R., Yoshikawa, K., Terui, F., Nakazawa, S., Tanaka, S., Saiki, T., Yoshikawa, M., Watanabe, S., Tanda, Y., 2021. Preliminary analysis of the Hayabusa2 samples returned from C-type asteroid Ryugu. Nat. Astron. 6, 214–220. https://doi.org/10.1038/s41550-021-01550-6

Yamada, M., Sasaki, S., Nagahara, H., Tsujiwara, A., Hasegawa, S., Yano, H., Hiroi, T., Ohashi, H., Otake, H., 1999. Simulation of space weathering of planet-forming materials: Nanosecond pulse laser irradiation and proton implantation on olivine and pyroxene samples. Earth Planets Sp. 51, 1255–1265.

Zinkle, S.J., 2012a. Effect of H and He irradiation on cavity formation and blistering in ceramics. Nucl. Instruments Methods Phys. Res. Sect. B Beam Interact. with Mater. Atoms 286, 4–19. https://doi.org/10.1016/j.nimb.2012.03.030

Zinkle, S.J., 2012b. Radiation-Induced Effects on Microstructure, in: Konings, R.J.M. (Ed.), Comprehensive Nuclear Materials. Elsevier, Amsterdam, pp. 65–98. https://doi.org/10.1016/B978-0-08-056033-5.00003-3

Zolensky, M., Barrett, R., Browning, L., 1993. Mineralogy and composition of matrix and chondrule rims in carbonaceous chondrites. Geochim. Cosmochim. Acta 57, 3123–3148. https://doi.org/10.1016/0016-7037(93)90298-B

Declaration of interests

☒ The authors declare that they have no known competing financial interests or personal relationships that could have appeared to influence the work reported in this paper.

☐The authors declare the following financial interests/personal relationships which may be considered as potential competing interests:

Highlights:

- A set of low flux and high flux 1 keV/amu H^+ and He^+ irradiation experiments were performed on the Murchison meteorite to investigate how the flux of solar wind affects space weathering of carbonaceous asteroidal regoliths
- XPS analyses show minor removal of surface carbon content and the chemical reduction of iron from its ferric to ferrous oxidation state
- Slope bluing is observed in irradiated VNIR spectra which may reflect carbonization/dehydrogenation of organic species
- No strong flux-dependence on the crystallinity of ion-damaged olivine is observed; higher He^+ flux may promote amorphization of phyllosilicates
- Ion-damaged surfaces in matrix samples are compositionally indistinct from unaltered matrix material; Mg and Si segregation is commonly observed in all olivine samples